

Adjoint based shape optimization in complex internal flows



Petr Kungurtsev

Supervisor: Prof. M. P. Juniper

Advisor: Dr. G. N. Wells

Department of Engineering
University of Cambridge

First year report

For my wife and parents

Declaration

I hereby declare that except where specific reference is made to the work of others, the contents of this dissertation are original and have not been submitted in whole or in part for consideration for any other degree or qualification in this, or any other university. This dissertation is my own work and contains nothing which is the outcome of work done in collaboration with others, except as specified in the text and Acknowledgements. This dissertation contains fewer than 20,000 words including appendices, bibliography, footnotes, tables and equations and has fewer than 150 figures.

Petr Kungurtsev
August 2017

Acknowledgements

I would like to greatly acknowledge my supervisor, Professor Matthew Juniper, for his full support. His inestimable guidance helped me to survive this year and learn his philosophy of how research should be done.

I am very thankful to my colleagues and friends Jack Brewster, Hans Yu and Jose Aguilar for many interesting discussions and feedback. I have never had such a friendly atmosphere and productive work environment.

Finally, Sveta has always been my guiding star. I can't appreciate her support and inspiration enough.

Abstract

A drop-on-demand inkjet printhead is a narrow, ink-filled, channel with a piezoelement on the upper boundary and a nozzle on the opposite side. The piezoelement oscillates, pushing a small amount of fluid through the nozzle to create a droplet, and acoustic waves propagate inside the channel. The printing speed depends on the rate at which droplets are expelled and therefore on the frequency of the boundary oscillation. As the frequency increases and approaches the first natural mode, the amplitude of the acoustic wave increases rapidly. As the previous pulse's acoustic waves have not decayed by the start of the next pulse, this leads to an unpredictable oscillatory behaviour inside the channel and print quality reduction. We aim to adjust the printhead geometry to increase the decay rate of acoustic oscillations, which should maintain print quality for higher frequencies.

The incompressible Navier–Stokes and viscous acoustic equations govern the flow dynamics inside the printhead. Using the adjoint approach, we calculate the mean flow viscous dissipation and acoustic eigenvalues sensitivities with respect to the shape of the domain. We apply the decay rate gradient in Hadamard form to change the Bezier-parameterized boundary shape, and modify the channel's geometry to increase the decay rate of acoustic fluctuations. Also, the presence of the domain boundaries compliance is taken into account to consider their deformation under the influence of acoustic waves.

Finally we demonstrate the developed computational tool which consists of an automated geometry and mesh generator, an unsteady incompressible solver, and a spectral solver for viscous acoustic flow, and adjoint solvers for shape gradients calculation.

Table of contents

List of figures	xiii
1 Introduction	1
1.1 Adjoint approach and shape optimization	1
1.2 Inkjet printers	3
1.3 Report structure	5
2 Viscous acoustic flow	7
2.1 Equations of motion	7
2.2 Equations of motion in the low Mach number limit	8
2.2.1 Nondimensionalization	9
2.2.2 Flow values expansion	10
2.3 Mean flow in the low Mach number limit	14
2.3.1 Problem statement	14
2.3.2 Weak formulation	15
2.3.3 Newton method	16
2.3.4 Unsteady mean flow	17
2.4 Acoustic flow in low Mach number limit	18
2.4.1 Problem statement	18
2.4.2 Weak formulation	19
2.4.3 Boundary conditions	20
2.4.4 Compliant boundary	23
3 Adjoint based shape optimization	27
3.1 Introduction to shape calculus	28
3.2 Pedagogical one-dimensional optimization	30
3.2.1 Burgers equation: sensitivity to control parameters	30
3.2.2 Shape optimization of linear acoustic problem	32

3.3	Adjoint for incompressible Navier–Stokes equation	36
3.3.1	Governing equations	36
3.3.2	Adjoint initial and boundary conditions	37
3.3.3	Shape derivative and Hadamard structure	39
3.3.4	Euler method for time-dependent adjoint system	40
3.4	Adjoint viscous acoustic problem	42
3.4.1	Governing equations	42
3.4.2	Adjoint boundary conditions	43
3.4.3	Shape derivative and Hadamard structure	44
3.5	Taylor testing for adjoint gradient	47
4	Applications	51
4.1	Computational methods	51
4.2	Shape optimization for stability	53
4.2.1	General approach	53
4.2.2	Spectrum-based optimization	57
4.3	Multi-objective shape optimization	59
4.3.1	General principle	59
4.3.2	Pareto optimality	60
4.3.3	Approaching Pareto frontier	62
4.4	Inkjet printhead optimization	64
4.4.1	Generic geometry	64
4.4.2	Optimization results	65
4.5	Shape optimization for viscous dissipation	69
5	Conclusion	71
5.1	Key results	71
5.2	Future research	72
	References	75
	Appendix A Shape parameterization	79
A.1	Motivation	79
A.2	General properties	79
A.3	Constructing a Bezier boundary	80
	Appendix B Complex eigenvalue problem in FEniCS	81

List of figures

1.1	Inkjet drop-on-demand print cycle.	4
3.1	Taylor tests of adjoint gradients for three cases: mismatching adjoint and finite difference gradients (Case 1), matching gradients (Case 2), and matching gradients with nonlinear terms dominating (Case 3). . .	48
4.1	Symmetric restriction part of the generic inkjet geometry as an optimization boundary.	53
4.3	Spectra of the channel for different shapes. Black dots correspond to the initial and the final eigenvalues, with intermediate steps in between. Arrows illustrate the direction of the spectrum shift.	55
4.4	Amplitude of the density variable, $ \hat{\rho} $, for the four modes (from top to bottom) for various channel's shapes. Left column: unperturbed channel; right column: the final shape.	55
4.5	Taylor tests for no slip boundary eigenvalue gradient, with quadratic and linear fitting.	56
4.6	Taylor tests for stress free boundary eigenvalue gradient, with quadratic and linear fitting.	56
4.7	Taylor tests for compliant boundary eigenvalue gradient, with quadratic and linear fitting.	57
4.8	Gradients of two objective functions J_1, J_2 with non-zero angle ϕ between the gradient directions (dashed lines) form a positive gradient subspace (green area), such that a possible gradient step exists which improves both the objectives.	60
4.9	Isolines of two functions intersect and create a region with a local Pareto frontier inside it. Two projected gradient vectors bound the area inside which both J_1 and J_2 increase.	61

4.10	Symmetric channel with two asymmetric restrictions. Black dots and dashed lines illustrate initial position of control points and smooth boundaries; red show those after a gradient step was applied.	62
4.11	Normalized gradient directions for viscous dissipation (green dots) and real part of the first eigenvalue (red dots) for four control points of the restriction boundaries.	63
4.12	The Xaar 1003 AMp printhead [42].	64
4.13	Generic geometry of the inkjet printhead (top and side view). Straight shaded lines correspond to no slip or compliant boundaries, dashed lines are planes of symmetry, and free boundaries as specified. Two red dotted lines denote restriction boundaries subject to optimization. All sizes in $100\mu\text{m}$	65
4.14	Initial channel geometry and the lowest frequency mode.	66
4.15	Channel geometry with the optimized left hand side constriction and the lowest frequency mode.	67
4.16	Channel geometry with two optimized constrictions and the lowest frequency mode.	67
4.18	Inlet velocity profile, viscous dissipation and shape gradient of unsteady flow in a channel. Shaded area illustrates the proposed averaging interval for periodic flow.	69
5.1	Gantt chart	73

Chapter 1

Introduction

1.1 Adjoint approach and shape optimization

Many problems in mathematical physics can be written in the form: given an operator A , find a solution u such that $Au = f$. In practice, one is usually interested in a value of linear functional (l, u) instead of the solution u itself. Introducing an adjoint operator, A^\dagger , related to the functional as $A^\dagger v = l$, the relation holds:

$$(l, u) = (l, A^{-1}f) = ((A^{-1})^\dagger l, f) = (v, f) \quad (1.1)$$

Thus, instead of solving the *direct* problem for different source terms f , it is only necessary to solve the *adjoint* problem once and calculate a linear functional (v, f) . This concept can be extended to differential operators and optimization problems in particular.

Consider an objective functional \mathcal{J} of a state \mathbf{q} , which we want to minimize. The state is governed by a system of partial differential equations and a set of parameters \mathbf{a} from an admissible parameter space \mathbf{A} .

$$\text{minimize } \mathcal{J}(\mathbf{q}, \mathbf{a}) \quad (1.2a)$$

$$\text{subject to } \mathbb{R}(\mathbf{q}, \mathbf{a}) = 0, \quad (1.2b)$$

$$\mathbf{a} \in \mathbf{A} \quad (1.2c)$$

The parameters can govern the initial or boundary conditions of the system, or the geometry of the problem. In particular, if positions of the boundary points are considered as the parameters themselves, i.e. explicitly define the shape optimization

problem, it is referred as parameter-free optimization. Otherwise, the geometry is constructed by a set of a design values, and the optimization problem becomes parameter-based.

Evaluation of the cost function at a given point $\tilde{\mathbf{a}}$ in the parameter space requires knowing the solution $\mathbf{q}(\tilde{\mathbf{a}})$. Once we want to find an optimal solution, a number of computationally expensive searches could be performed around the current state, namely one state calculation for each adjustable parameter: $\mathbf{q}(a_1, a_2, \dots, a_n + \Delta a_n, \dots, a_N)$. In industrial applications, however, the direct calculation of gradient information can be extremely costly, especially when the number of control parameters is large or every trial is expensive. Consequently, adjoint-based methods [16] become promising for engineering design and shape optimization. Adjoint method allows to calculate sensitivities with respect to each parameter by only one state calculation and N linear computation to obtain $\frac{d\mathcal{J}}{da_n}, n = 1, \dots, N$.

First, let us consider the full cost function and the state equations derivative:

$$\frac{d\mathcal{J}}{da_n} = \frac{\partial \mathcal{J}}{\partial \mathbf{q}} \frac{\partial \mathbf{q}}{\partial a_n} + \frac{\partial \mathcal{J}}{\partial a_n}, \quad (1.3a)$$

$$\frac{d\mathbb{R}}{da_n} = \frac{\partial \mathbb{R}}{\partial \mathbf{q}} \frac{\partial \mathbf{q}}{\partial a_n} + \frac{\partial \mathbb{R}}{\partial a_n} = 0 \quad (1.3b)$$

Second, we introduce co-state (adjoint) variable λ and construct the Lagrangian of the system:

$$\mathcal{L} = \mathcal{J} - (\lambda, \mathbb{R}(\mathbf{q}, \mathbf{a})) \quad (1.4)$$

Due to the arbitrary nature of λ , we can choose it to satisfy

$$\frac{\partial \mathcal{L}}{\partial \mathbf{q}} \delta q = 0 = \frac{\partial \mathcal{J}}{\partial \mathbf{q}} \delta q - \left(\lambda, \frac{\partial \mathbb{R}}{\partial \mathbf{q}} \delta q \right), \quad (1.5a)$$

$$\Rightarrow \frac{\partial \mathcal{J}}{\partial \mathbf{q}} \delta q = \left(\lambda, \frac{\partial \mathbb{R}}{\partial \mathbf{q}} \delta q \right) \quad (1.5b)$$

Using the definition of the adjoint:

$$\frac{\partial \mathcal{J}}{\partial \mathbf{q}} \delta q = \left(\frac{\partial \mathbb{R}^\dagger}{\partial \mathbf{q}} \lambda, \delta q \right) \quad (1.6)$$

And therefore, the objective function gradient with respect to parameters

$$\frac{d\mathcal{J}}{da_n} = \frac{\partial\mathcal{J}}{\partial a_n} + \left(\lambda, \frac{\partial\mathbb{R}}{\partial\mathbf{q}} \frac{\partial\mathbf{q}}{\partial a_n} \right) = \frac{\partial\mathcal{J}}{\partial a_n} - \left(\frac{\partial\mathbb{R}^\dagger}{\partial\mathbf{q}} \lambda, \frac{\partial\mathbf{q}}{\partial a_n} \right) \equiv \frac{\partial\mathcal{L}}{\partial a_n} \quad (1.7)$$

By introducing a new variable, we eliminated parameter sensitivities of the state equation, i.e. the so-called grid sensitivity. Now, to calculate the objective gradient, we only require one solution of the state equation (1.2b), one solution of the adjoint equation (1.5b), and N evaluations of (1.7), which are cheap.

In present research we apply the continuous adjoint method: the adjoint state equations are derived analytically and then discretized [17], and we obtain a discrete approximation of the objective function gradient, $(\nabla\mathcal{J})_h$. Another approach, the discrete adjoint method, applies the adjoint operator on the already discretized equations, which provides us with an exact gradient of the approximated objective function $\nabla(\mathcal{J}_h)$.

Parameter-based shape optimization is based on the concept that for each control point \mathbf{a} there is a displacement field, $\mathbf{V}_\mathbf{a}$, and a change of the system parameter results in the geometry transformation in the direction of the displacement field. It can be shown, that for admissible objective functions the gradient can be written in Hadamard form [6]:

$$\frac{d\mathcal{J}}{da_n} = \int_{\partial\Omega} \mathbf{V}_{a_n} \mathbf{G}(\mathbf{q}, \lambda) d\Gamma \quad (1.8)$$

Applying the continuous adjoint approach, we seek an analytic expression for $\mathbf{G}(\mathbf{q}, \lambda)$, and integrate this function over the optimization boundary to calculate the objective shape sensitivity.

1.2 Inkjet printers

Inkjet drop-on-demand printing is a type of printing which recreates an image by propelling droplets of ink onto substrate, for example, paper. The way a droplet is formed depends on the printing technology. One of the most common are thermal and piezo inkjet printers. Thermal inkjet printers contain a resistive heater to create a vapor bubble that pushes the fluid [25]. Piezo electric inkjet technology applies a control electric pulse to a piezo-element, which vibrates and sets the ink fluid inside the printhead into motion. This printing technology is very popular due to its precision and operational speed: the droplet size can start from 1 pl, and the frequency of the ink jetting reaches 50kHz, or even more [42]. Target frequency, which we want to achieve, is in order of several hundred kilohertz.

A printhead is in general a channel filled with ink, with a small nozzle on the bottom and a piezoelectric element at the top. There is a slow flow through the channel, which maintains the ink volume inside. The piezoelement acts as an oscillator and creates acoustic waves inside the channel. We can distinguish three consecutive droplet formation stages. At stage 1 (fig. 1.1a), piezo element is undeformed. An electric trapezoid impulse is applied to it, which displaces the top boundary and pushes ink through the nozzle. At stage 2 (fig. 1.1b), the piezo bends which forms pressure waves and a droplet appears at the orifice. Finally, at stage 3 (fig. 1.1c), piezoelement deforms back and a single drop is created. At the same time, acoustic waves continue to propagate inside the channel, which can lead to undesired effects, such as formation of satellite drops.

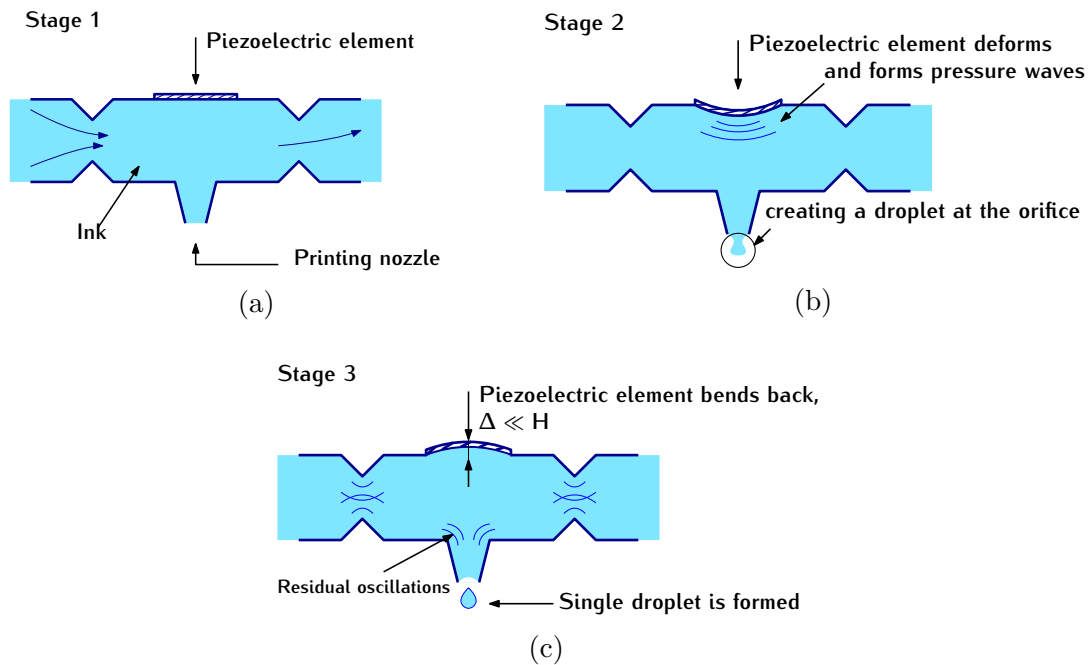


Fig. 1.1 Inkjet drop-on-demand print cycle.

These residual oscillations inside the channel have been called the primary performance limiting factor [20]. The main question is how can one dump these residual oscillations or make them propagate out of the channel? There are several studies on wave propagation in inkjet printers [1] and performance optimization [23], based on feed-forward control, for example, the shape of electric signal [19]. They attempted to improve the system's response to high frequency boundary oscillations, namely the transfer function $H(q) : q \rightarrow y$, which relates the piezo input voltage q to the meniscus (the liquid-air interface at the orifice) velocity y .

The meniscus dynamics and the subsequent droplet formation are another important processes. This is a multiphase physical phenomena, involving liquid-solid interaction on the nozzle surface (wetting and contact angle) [41], and liquid-gas interaction that involves the dynamics of the interface shape and surface tension [40]. In this report, we are going to focus on the shape optimization of the channel, omitting the multiphase effects at the nozzle boundary.

1.3 Report structure

The report consists of four chapters, including introduction. In chapter 2, we derive two limits of the compressible Navier–Stokes equation. We perform a two-parameter expansion to split the full problem into the incompressible mean flow and viscous acoustic flow. Then, we obtain a weak formulation for these two limits, and extend the concept of the compliant boundary type to the viscous case. In chapter 3, we state the optimization problem, aiming to minimize viscous dissipation of the unsteady mean flow, and stabilize the acoustic flow by increasing the decay rate of natural modes. Starting with one-dimensional optimization examples, we overview the Lagrangian approach and construct the adjoint-based shape gradient of the objective functions in Hadamard form. Chapter 4 contains applications of the present method, in particular shape optimization of a simplified geometry (a two-dimensional channel with adjustable restriction) and a generic printhead geometry. We continue with coupling the viscous dissipation and stability optimization problems and discuss the process of multiobjective optimization.

Chapter 2

Viscous acoustic flow

In this chapter we start with the review of the fully compressible Navier–Stokes equations and aim to derive two limit cases: incompressible flow and acoustic flow equations from the power expansion of the initial problem assuming that the flow is governed by some low characteristic numbers. We will see that in the case of low Mach number of the base and fluctuating flows the initial problem can be split into two sub-problems. Then, we discuss both the strong and the weak forms for each of two cases; finally, we consider possible boundary conditions and their implementation.

2.1 Equations of motion

The full compressible Navier–Stokes equations govern the motion of a fluid with the presence of viscous effects, heat conductivity, compressibility and external body forces. In general, the equations in conservative form are given by [24]:

$$\frac{\partial}{\partial t} \mathbf{q} + \frac{\partial}{\partial x_k} (\mathbf{f}_k^c(\mathbf{q}) - \mathbf{f}_k^v(\mathbf{q}, \nabla \cdot \mathbf{q})) = 0 \quad \text{in } \Omega \quad (2.1)$$

Here we use ^c and ^v referring to convective and viscous parts of the equations. The vector of conservative variables \mathbf{q} and the fluxes $f^c(\mathbf{q}), f^v(\mathbf{q})$ are defined by

$$\mathbf{q} = \begin{bmatrix} \rho \\ \rho u_1 \\ \rho u_2 \\ \rho E \end{bmatrix}, \quad f_k^c(\mathbf{q}) = \begin{bmatrix} \rho u_k \\ \rho u_1 u_k + P \delta_{1k} \\ \rho u_2 u_k + P \delta_{2k} \\ \rho u_k H \end{bmatrix}, \quad f_k^v(\mathbf{q}) = \begin{bmatrix} 0 \\ \tau_{k1} \\ \tau_{k2} \\ \tau_{kj} u_j + \partial_k \kappa T \end{bmatrix} \quad (2.2)$$

The viscous stress tensor τ_{ij} is proportional to the dynamic viscosity coefficient μ and equals to

$$\tau_{ij} = \mu \left(\nabla_i u_j + \nabla_j u_i - \frac{2}{3} \text{div}(\mathbf{u}) \delta_{ij} \right) \quad (2.3)$$

Introduced variables ρ, \mathbf{u}, P, E and H denote the density, velocity vector, pressure, total energy and enthalpy of the flow:

$$P(\mathbf{q}) = (\gamma - 1)\rho e, \quad (2.4a)$$

$$\rho E = \rho e + \frac{\rho \mathbf{u}^2}{2}, \quad (2.4b)$$

$$H(\mathbf{q}) = \frac{\rho E + P}{\rho} \quad (2.4c)$$

Static internal energy e is related to the temperature T of the flow by $e = c_v T$, where c_v denotes the constant volume heat capacity. We can define the Prandtl number $Pr = \frac{\mu \gamma c_v}{\kappa}$, κ is the thermal conductivity coefficient. For example, in the case of an ideal gas, a Prandtl number $Pr = 0.72$. We also need to introduce an equation of state, which relates the pressure, density and temperature, i.e. $\rho = \rho(P, T)$.

Usually, solving these equations is a challenge itself, including choosing an appropriate discretization and numerical methods, which is another noticeable research area. For example, discontinuous Galerkin finite element method [14] is a promising candidate to solve the full problem.

2.2 Equations of motion in the low Mach number limit

Now, let us introduce two parameters to describe the flow. Here we follow the results presented in [27] for the low Mach number asymptotics of the Navier–Stokes equations, and [5] for two-parameter expansion derivation.

First, consider that we have a steady fluid flow in a channel with rigid boundaries, and the mean inlet velocity is in order of 1 – 10 m/s. Then the Mach number of the base mean flow can be characterized by a small parameter, $\mu = M^b$, since the velocity of the flow is much smaller than the speed of sound $c_s^b = \sqrt{\gamma P^b / \rho^b}$, such that the local Mach number is:

$$M = \frac{u}{\sqrt{\gamma P^b / \rho^b}} = \frac{u}{u^b} M^b \rightarrow 0 \quad \text{if} \quad M^b \rightarrow 0 \quad (2.5)$$

where b corresponds to the reference base dimensional values describing the flow. We choose the reference quantities such that the u/u^b is in order of $\mathcal{O}(1)$.

Second, the flow is perturbed by small boundary oscillations created by a piezo-element. These fluctuations are created at the boundary and propagate inside the channel. The inkjet printing device is designed to create a sequence of small droplets jetting through a tiny orifice, and these oscillations are the primal mechanism of droplets formation at the nozzle outlet boundary [25]. Although the boundary displacement is assumed to be negligibly small, acoustic waves form inside the channel and represent an additional physical phenomenon to be studied. This type of fluctuating motion should be small in comparison to the mean quantities, and moreover be described by another parameter. Introducing a new small characteristic number, ε , we will use it to define the Mach number of the fluctuating flow.

These two small parameters, μ and ε , represent different physical phenomena. Consequently, the formal expansion of the governing equations will give us terms with different orders in μ, ε : $\mathcal{O}(\mu^{k_1} \varepsilon^{k_2})$, where k_1, k_2 are some integer numbers (e.g., $k_2 = 0$ for a flow with no oscillations). This generally characterizes the flow processes. For example, as will be shown later, setting ε to zero and collecting terms of $\mathcal{O}(\mu)$ leads to the well-known momentum equation of an incompressible flow.

2.2.1 Nondimensionalization

To perform the following analysis of the low Mach number limit of the equations of motion, it is necessary to define the nondimensional variables. New equations will include dimensionless quantities such as the Reynolds number (if the flow is viscous), the Froude number (if gravity is included into the model), or, for instance, those related to the considered forces acting on the flow.

Dimensional reference quantities can be based on the far-field conditions, but in the case of the internal flow it seems more natural to refer to the steady flow state without mean flow: $\rho^b, T^b, c_s^b, \mu^b$ (reference density, temperature, speed of sound and viscosity) and a domain size L as a reference length scale. The reference pressure P^b used here is chosen as a function of density and speed of sound: $P^b = \rho^b (c_s^b)^2$. Hence a new set of variables becomes:

$$\frac{\rho}{\rho^b} \rightarrow \rho, \quad \frac{P}{P^b} \rightarrow P, \quad \frac{T}{T^b} \rightarrow T, \quad \frac{u}{c_s^b} \rightarrow u \quad (2.6a)$$

$$\frac{E}{P^b/\rho^b} \rightarrow E, \quad \frac{H}{P^b/\rho^b} \rightarrow H, \quad (2.6b)$$

$$\frac{x}{L} \rightarrow x, \quad \frac{t}{L/c_s^b} \rightarrow t \quad (2.6c)$$

The dimensionless parameters such as the Reynolds number appear in the equations at this stage, with $Re = \rho^b c_s^b L / \mu^b$. These values depend on the choice of the reference values.

While some approaches [5] are based on the speed of sound dimensionalization, also in some cases choosing a known velocity of the flow (for example, at the inlet) as a reference quantity helps obtaining slightly different and more demonstrative results, such as temporal multiple scales analysis [27]. However, this approach is not suitable if the inlet velocity is zero, whilst the speed of sound is never a small quantity. We will use speed of sound as a reference velocity for the compressible flow, and the non-zero inlet velocity in the incompressible case.

2.2.2 Flow values expansion

As discussed before, physical processes in the flow arise from two different sources: the mean flow characterized by the parameter μ and the fluctuating flow related to the second parameter ε . We can then write the flow state \mathbf{q} as a sum of mean values $\bar{\mathbf{q}}$ and fluctuating values $\tilde{\mathbf{q}}$:

$$\rho = \bar{\rho} + \tilde{\rho}, \quad u = \bar{u} + \tilde{u}, \dots \quad (2.7)$$

Referring back to the original idea of two parameters analysis, fluctuating values should be of the order in amplitude ε , while some mean values are in order of 1, not μ . For instance, consider the no-mean flow configuration when $\mu = 0$, so the dimensional flow density becomes $\rho = \rho^b = \mathcal{O}(1)$.

We substitute (2.7) into the full system of compressible Navier–Stokes equations (2.1) and gather terms which have the same order of magnitude. We want to keep only the leading terms in μ, ε , i.e. non-zero and non-trivial terms. The rest of the terms represents the combination of the mean and fluctuating flow with terms containing both Mach numbers, thus describes the interactions between these two physical processes. The split mass and momentum conservation equations become:

$$[\partial_t \bar{\rho} + \nabla_i(\bar{\rho} \bar{u}_i)] + [\partial_t \tilde{\rho} + \nabla_i(\bar{\rho} \tilde{u}_i)] + \mathcal{O}(\varepsilon^2, \varepsilon\mu, \dots) = 0 \quad (2.8)$$

$$\left[\partial_t(\bar{\rho} \bar{u}_i) + \nabla_j(\bar{\rho} \bar{u}_i \bar{u}_j) + \nabla_i \bar{P} - \frac{1}{Re} \nabla_j \bar{\tau}_{ij} \right] + \left[\partial_t(\bar{\rho} \tilde{u}_i) + \nabla_i \tilde{P} - \frac{1}{Re} \nabla_j \tilde{\tau}_{ij} \right] + \mathcal{O}(\varepsilon^2, \varepsilon\mu, \dots) = 0 \quad (2.9)$$

The first bracket in both (2.8) and (2.9) contains only terms related to the mean state $\bar{\mathbf{q}}$, and the second bracket gathers the fluctuating quantities $\tilde{\mathbf{q}}$.

Direct consideration of the first bracket in (2.8) shows that all terms are proportional to the first power of μ : mean density $\bar{\rho}$ has the leading term of $\mathcal{O}(1)$ as shown before, the temporal derivative is proportional to μ since the speed of sound was chosen to nondimensionalize it (it can be clearly seen from (2.6) that by choosing u^b instead of c_s^b as a reference velocity quantity results in the $u^b/c_s^b = \mathcal{O}(\mu)$ term appearing). Consequently, all terms in the first bracket of (2.8) are $\mathcal{O}(\mu^1)$. Let us denote the terms proportional to the zeroth order of Mach number as $\bar{\rho}_0, \bar{u}_{i,0}$, to the first order as $\bar{\rho}_1, \bar{u}_{i,1}$, and so on.

$$\partial_t \bar{\rho}_0 + \nabla_i(\bar{\rho}_0 \bar{u}_{i,1}) = 0 \quad (2.10)$$

The first bracket in (2.9) shows that all terms are proportional to the second power of μ , except the pressure gradient, which should be in order of $\mathcal{O}(1)$. To understand this seeming discrepancy, let us follow [27] and expand pressure in power series of μ :

$$\bar{P} = \bar{P}_0 + \bar{P}_1 + \bar{P}_2 + \mathcal{O}(\mu^3) \quad (2.11)$$

Now, applying this expansion to the first bracket of (2.9) and gathering terms with the same power of the small parameter gives:

$$\mu^0 : \nabla_i \bar{P}_0 = 0, \quad (2.12a)$$

$$\mu^1 : \nabla_i \bar{P}_1 = 0, \quad (2.12b)$$

$$\mu^2 : \partial_t(\bar{\rho}_0 \bar{u}_{i,1}) + \nabla_j(\bar{\rho}_0 \bar{u}_{i,1} \bar{u}_{j,1}) + \nabla_i \bar{P}_2 - \frac{1}{Re} \nabla_j \bar{\tau}_{ij,1} = 0 \quad (2.12c)$$

Now, it becomes clear that the zeroth and first order pressure terms are related to the total energy density and act like a thermodynamic pressure. The second order term \bar{P}_2 plays a similar role as the pressure in the incompressible Navier–Stokes equation.

Performing similar analysis for the energy equation and considering the mean flow quantities behavior, we obtain the well-known heat equation:

$$\bar{\rho}_0 \partial_t \bar{T}_0 - \nabla_j \kappa \nabla_j \bar{T}_0 = 0 \quad (2.13)$$

We assume there is no external heating thus the zeroth-order temperature is constant.

To finally derive the incompressible Navier–Stokes equation, assume that the variation of density and temperature of the flow is small in comparison to the no-flow state, $\|\delta\bar{\rho}\| = \|\bar{\rho} - \rho^b\| \ll \|\rho^b\|$, or, in other words, $\delta\bar{\rho} = \mathcal{O}(\mu)$. This leads us to the Boussinesq buoyancy equations [34], which to the lowest order in μ results in:

$$\text{div}(\bar{u}) = 0, \quad (2.14a)$$

$$\bar{\rho} \partial_t(\bar{u}_i) + \bar{\rho}(\bar{u}_j \nabla_j) \bar{u}_i + \nabla_i \bar{P}_2 - \frac{1}{Re} \nabla_j \tilde{\tau}_{ij} = 0 \quad (2.14b)$$

The second brackets in (2.8) and (2.9) are the acoustic motion of the flow; terms are proportional to ε and do not contain information about the mean flow. Since the first bracket terms were shown to be zero, we can conclude that the second bracket terms should also be zero, leading us to the equations of linear acoustics:

$$\partial_t \tilde{\rho} + \bar{\rho} \text{div}(\tilde{u}) = 0, \quad (2.15a)$$

$$\bar{\rho} \partial_t(\tilde{u}_i) + \nabla_i \tilde{P} - \frac{1}{Re} \nabla_j \tilde{\tau}_{ij} = 0 \quad (2.15b)$$

The energy production term in (2.2) proportional to viscosity is in order of u^2 and can be neglected while considering expansion to the first order of ε . The energy density variable ρE is equivalent to internal energy $\rho e = P/(\gamma - 1)$ up to the the first order of ε , so the energy conservation equation can be formulated in terms of pressure. Gathering the first order fluctuating values in the energy equation yields:

$$\frac{1}{\gamma - 1} \partial_t \tilde{P} + \frac{\gamma}{\gamma - 1} \nabla_i (\tilde{u}_i \bar{P}_0) - \nabla_j \kappa \nabla_j \tilde{T} = 0 \quad (2.16)$$

By definition, temperature T equals to $\frac{P}{\rho c_v(\gamma - 1)}$, thus the temperature fluctuation is:

$$\tilde{T} = \frac{1}{c_v(\gamma - 1)} \left(\frac{\tilde{P}}{\rho} \right) = \frac{1}{c_v(\gamma - 1)} \frac{\bar{P}_0}{\bar{\rho}} \left(\frac{\tilde{P}}{\bar{P}_0} - \frac{\tilde{\rho}}{\bar{\rho}_0} \right) \quad (2.17)$$

Now the first order energy equation becomes:

$$\partial_t \tilde{P} + \gamma \bar{P}_0 \operatorname{div}(\tilde{u}) - \frac{1}{c_v} \frac{\bar{P}_0}{\bar{\rho}} \nabla_j \kappa \nabla_j \left(\frac{\tilde{P}}{\bar{P}_0} - \frac{\tilde{\rho}}{\bar{\rho}_0} \right) = 0 \quad (2.18)$$

Now, if we assume that the flow is isentropic $\tilde{P} = c_s^2 \tilde{\rho}$, then using the speed of sound definition $c_s^b = \sqrt{\gamma P^b / \rho^b}$ the energy (pressure) equation degenerates to the mass conservation equation in (2.15).

Summing up, that the problem can be separated in two smaller problems: incompressible mean flow and linear acoustics, only due to the fact that we assumed terms of $\mathcal{O}(\varepsilon^2, \varepsilon\mu, \dots)$ to be small and therefore we neglect the interaction between the mean flow and the fluctuating flow. Otherwise, mean state $\bar{\mathbf{q}}$ and fluctuating state $\tilde{\mathbf{q}}$ are coupled through the higher order terms which represent mass, momentum and energy transfer between them.

2.3 Mean flow in the low Mach number limit

Low Mach number expansion of the Navier–Stokes equations results in the mass and momentum conservation laws of incompressible base flow and classical linear acoustic problem. In this section we consider both steady and unsteady incompressible flow and briefly discuss the governing equations and weak formulation.

2.3.1 Problem statement

Incompressible Navier–Stokes equation can be considered as an equation of motion plus a constraint, that makes the flow divergenceless. The pressure variable is not directly related to the thermodynamic state, and adjusts in a way that the velocity constraint is satisfied. The governing equations are:

$$\frac{\partial u_i}{\partial t} + (u_j \nabla_j) u_i + \nabla_i P - \frac{1}{Re} \Delta u_i = 0, \quad (2.19a)$$

$$\operatorname{div}(u) = 0 \quad (2.19b)$$

This dimensionless form contains a characteristic Reynolds number Re , which defines the flow behaviour. Previously, speed of sound was used as a reference speed; however, in this case it is necessary to dimensionalize velocity by some known value related to the base flow itself, for example, inlet velocity, since there is no meaningful sound speed. Then, Reynolds number is defined as $Re = \frac{\rho U_{in} L}{\mu}$.

We consider four types of boundary conditions:

- Inlet boundary

Velocity is prescribed at the inlet boundary, but not pressure. This is Dirichlet boundary condition, namely:

$$u = U_{in} \quad \text{on} \quad \Gamma_{in} \quad (2.20)$$

- No slip boundary

No slip boundary imposes no flow through the wall, and adhesion condition for viscous flows. Then, both normal and tangential velocity components are zero and the no slip Dirichlet boundary condition becomes:

$$u = 0 \quad \text{on} \quad \Gamma_{nsl} \quad (2.21)$$

- Slip boundary

In some cases, for example if fluid is inviscid or a symmetry plane is modelled, slip wall boundary condition is required:

$$u_n = 0 \text{ on } \Gamma_{nsl} \quad (2.22)$$

Here u_n is a normal component of the flow velocity. Slip boundary condition allows non-zero flow along the surface.

- Outlet boundary

Outlet, or no-stress boundary is used to model outflow. Since pressure appears only in the gradient term, it is defined up to some constant. Let us set the outer pressure to zero, then the stress-free condition turns into

$$n_j(P\delta_{ij} - \frac{1}{Re}\nabla_j u_i) = Pn_i - \frac{1}{Re}\frac{\partial u_i}{\partial n} = 0 \quad (2.23)$$

Additionally, in the case of unsteady flow, initial condition $u(x, t = 0)$ should be provided.

2.3.2 Weak formulation

Consider for now that the flow is steady, $\frac{\partial u_i}{\partial t} = 0$, and here we aim to construct a weak form of the reduced problem. Non-zero time derivative will be taken into account in the following section.

First, we multiply the incompressible Navier–Stokes equation (2.19a) by vector test function, v_i , and the divergence constraint (2.19b) by scalar function, q , and integrate both over the computational domain. Second, we integrate the highest order derivatives, $-\frac{1}{Re}\Delta u_i$ and $\nabla_i P$ by parts and collect all the integrals together. This leads to:

$$\left\langle v_i(u_j \nabla_j)u_i - P \operatorname{div}(v) + \frac{1}{Re}\nabla_j v_i \nabla_j u_i - q \operatorname{div}(u) \right\rangle + \left\{ v_i \left(Pn_i - \frac{1}{Re}\frac{\partial u_i}{\partial n} \right) \right\} = 0 \quad (2.24)$$

The boundary integral disappears completely due to the boundary conditions. Inlet and no slip Dirichlet boundaries result in $v = 0$ since the choice of test function is arbitrary. Slip boundary sets both u_τ, v_τ to zero and the remaining term vanishes due to the symmetry (or, equivalently, no shear stress at the boundary). Outlet boundary

condition is exactly the last boundary integral multiplied by some function, such that the last remaining term is zero everywhere.

Summing up, the weak form of the incompressible Navier–Stokes equation with the given boundary types contains only a volumetric integral, with Dirichlet boundary conditions for inlet, slip and no slip boundaries.

2.3.3 Newton method

The problem (2.19) is nonlinear, the convective term is proportional to u^2 . Let us recall the weak form (2.24) and a steady residual form $\mathbb{R}(q)$ is:

$$\mathbb{R}(q) = \left\langle v_i(u_j \nabla_j)u_i - P \operatorname{div}(v) + \frac{1}{Re} \nabla_j v_i \nabla_j u_i - q \operatorname{div}(u) \right\rangle \quad (2.25)$$

It should be zero if $q = (u, P)$ satisfies the incompressible Navier–Stokes equation. Consider we have an initial guess of the flow state $q_0 = (u_0, P_0)$, which can, for instance, be chosen zero everywhere or satisfy the linear Stokes equation. We employ a Newton method to solve the nonlinear system with a known initial guess. To find the next iterate we linearize the residual form by taking the Frechet derivative with respect to state q . Linearization of the Dirichlet boundary conditions is straightforward, which finally gives:

$$\mathbb{R}(q^{n+1}) = \mathbb{R}(q^n) + \frac{\partial \mathbb{R}}{\partial q} \delta q + \mathcal{O}(\delta q^2) \quad (2.26)$$

And the linearized weak problem becomes:

$$\left\langle v_i ((u_j \nabla_j) \delta u_i + (\delta u_j \nabla_j) u_i) - \delta P \operatorname{div}(v) + \frac{1}{Re} \nabla_j v_i \nabla_j \delta u_i - q \operatorname{div}(\delta u) \right\rangle = -\mathbb{R}(q^n) \quad (2.27)$$

Then the initial nonlinear problem turns into a linear system on δq . Setting (2.26) to zero and finding δq , we update the previous solution as $q^{n+1} = q^n + \delta q$ and calculate the l_2 -norm of the updated residual, $\|\mathbb{R}(q^{n+1})\|_2$. If the norm is less than the chosen tolerance, the process is stopped. Otherwise, we continue the convergence procedure.

A damped Newton method can be useful for some problems. It means, that the solution is updated by weighed step, $\alpha_w \delta q$, which is dynamically chosen to maintain better convergence rate. In present research, we used the undamped Newton algorithm.

2.3.4 Unsteady mean flow

Now, consider time-dependent Navier–Stokes equation, with a new residual form to be introduced:

$$\mathbb{N}(q(t)) = \left\langle v_i \frac{\partial u_i}{\partial t} \right\rangle + \mathbb{R}(q(t)) \quad (2.28)$$

There are several methods of solving the unsteady problem, for example, fractional step method [8]. However, we want to employ the existing solution of the steady problem, and we aim to derive an implicit scheme for time integration. The idea is to perform the temporal discretization first, and then reduce new system to previous case. The Euler approach presents time derivative as

$$\frac{\partial u}{\partial t} \rightarrow \frac{u^{n+1} - u^n}{\Delta t}$$

Here we perform time discretization as $t^k = k\Delta t$, where Δt is time step. The unsteady weak formulation then becomes:

$$\left\langle v_i \frac{u_i^{n+1}}{\Delta t} \right\rangle + \mathbb{R}(q^{n+1}) = \left\langle v_i \frac{u_i^n}{\Delta t} \right\rangle \quad (2.29)$$

This is still a nonlinear problem, and we follow the same strategy as for the steady problem. Taking the Frechet derivative of (2.29), the iterative scheme is given by:

$$\left\langle v_i \frac{\delta u_i}{\Delta t} + v_i ((u_j \nabla_j) \delta u_i + (\delta u_j \nabla_j) u_i) - \delta P \operatorname{div}(v) + \frac{1}{Re} \nabla_j v_i \nabla_j \delta u_i - q \operatorname{div}(\delta u) \right\rangle = \quad (2.30a)$$

$$-\mathbb{R}(q) + \left\langle v_i \frac{u_i^n - u_i}{\Delta t} \right\rangle \quad (2.30b)$$

Here linear system is solved for δq , u^n corresponds to the known velocity at the previous time step, and u_i is the velocity iterate updated as $u_i \rightarrow u_i + \delta u_i$ until the convergence criteria is met. As the right hand side (2.30b) goes to zero, a new solution is found for time t^{n+1} .

The advantage of this approach is only a little difference from the steady formulation. First, the time derivative term $v_i \frac{\delta u_i}{\Delta t}$ is added to the bilinear form, and second, the semi-time derivative $\frac{u_i^n - u_i}{\Delta t}$ appears on the linear form. Essentially, the solution process doesn't differ from that previously discussed.

2.4 Acoustic flow in low Mach number limit

In the previous sections we discussed the technique of splitting the initial set of compressible Navier–Stokes equations into two smaller problems, the incompressible mean flow and the acoustic flow, governed by two small parameters, μ and ε , respectively. Here we consider the acoustic, or the fluctuating flow created by an oscillating piezoelement boundary. We develop the general strong and weak formulation of the acoustic problem, types of boundary conditions relevant to the problem, to finally obtain the adjoint system and the stability sensitivity to the changes in shape.

2.4.1 Problem statement

We recall the result of the low Mach number expansion, and the linear acoustic equations (2.15) will be the primal object of interest. Since the viscous source term in the energy equation (2.2) is proportional only to the squared amplitude of the velocity $\mathcal{O}(u^2)$, this allows us to assume that the energy production due to the viscosity is small thus making our flow isentropic for the purpose of relating \tilde{P} to $\tilde{\rho}$. Note that we retain viscosity in the momentum equation, where it appears at first order in u . The isentropic flow property allows us to eliminate the pressure term in the momentum equation which in dimensional case is related to density through the speed of sound, c_s : $\nabla \tilde{P} = c_s^2 \nabla \tilde{\rho}$. Summing up, the remaining dimensional continuity and momentum equations are:

$$\partial_t \tilde{\rho} + \rho_0 \operatorname{div}(\tilde{u}) = 0, \quad (2.31a)$$

$$\rho_0 \partial_t \tilde{u}_i + c_s^2 \nabla_i \tilde{\rho} - \mu \left(\Delta \tilde{u}_i + \frac{1}{3} \nabla_i \operatorname{div}(\tilde{u}) \right) = 0. \quad (2.31b)$$

For the purpose of the stability analysis of the acoustic problem, instead of solving the unsteady problem we move to the frequency domain assuming solutions in form of $\tilde{\mathbf{q}}(x, t) = \hat{\mathbf{q}}(x) e^{st}$, such that $\partial_t(\rho', u') \rightarrow s(\hat{\rho}, \hat{u})$, where $\hat{\rho}, \hat{u}$ are complex amplitudes and s is a complex frequency of a mode. New dimensionless variables become: $\tilde{\rho}/\rho_0 \rightarrow \hat{\rho}, \tilde{u}_i/c_s \rightarrow \hat{u}_i, \mu/(\rho_0 c_s L) \rightarrow \nu \equiv Re^{-1}, sL/c_s \rightarrow s$. We look for a normal mode solution, so the eigenvalue problem can finally be written as:

$$-div(\hat{u}) = s\hat{\rho}, \quad (2.32a)$$

$$\nabla_i \hat{\rho} - \nu \left(\Delta \hat{u}_i + \frac{1}{3} \nabla_i div(\hat{u}) \right) = -s\hat{u}_i. \quad (2.32b)$$

The sign of the first equation becomes important for the symmetry of the weak form. The momentum equation can be rewritten in the form of the Newton's law, by introducing a new variable for the stress tensor $\hat{\sigma}_{ij} = -\hat{\rho}\delta_{ij} + \nu(\nabla_j \hat{u}_i + \nabla_i \hat{u}_j - 2/3\delta_{ij}div(\hat{u}))$. The divergence of the stress tensor is an acting force, thus

$$s\hat{u}_i = \nabla_j \hat{\sigma}_{ij} \quad (2.33)$$

Now the acceleration term on the left hand side equals to the force term on the right hand side. We will use the stress tensor notation while formulating the weak problem and the boundary conditions.

2.4.2 Weak formulation

Now, the weak form of the given dimensionless eigenvalue problem is introduced. Multiplying the first scalar equation by a scalar test function, w , and the momentum equation by a vector test function, v_i , and integrating over the domain we have:

$$\langle -div(\hat{u})w \rangle = \langle s\hat{\rho}w \rangle, \quad (2.34a)$$

$$\langle -v_i \nabla_j \hat{\sigma}_{ij} \rangle = \langle -s\hat{u}_i v_i \rangle \quad (2.34b)$$

After summation and integration by part the highest order derivatives once we will have several boundary integrals, namely:

$$\langle -div(\hat{u})w + \hat{\sigma}_{ij} \nabla_j v_i \rangle - \{v_i n_j \hat{\sigma}_{ij}\} = s \langle \hat{\rho}w - \hat{u}_i v_i \rangle. \quad (2.35)$$

The volumetric terms $\langle \dots \rangle$ and the boundary terms $\{ \dots \}$ of the weak form are not yet symmetric to the swap of the test functions to trial functions. We won't symmetrize

the boundary integrals at this point, but after the boundary conditions are considered. Regarding the volume integrals, from the symmetry of the stress tensor it is clear that:

$$\langle \hat{\sigma}_{ij} \nabla_j v_i \rangle = \left\langle \frac{1}{2} \hat{\sigma}_{ij} (\nabla_j v_i + \nabla_i v_j) \right\rangle = \quad (2.36a)$$

$$\left\langle -\hat{\rho} \operatorname{div}(v) + \frac{\nu}{2} \left(\nabla_j \hat{u}_i + \nabla_i \hat{u}_j - \frac{2}{3} \delta_{ij} \operatorname{div}(\hat{u}) \right) (\nabla_j v_i + \nabla_i v_j) \right\rangle = \quad (2.36b)$$

$$\left\langle -\hat{\rho} \operatorname{div}(v) + \frac{\nu}{2} \left(\nabla_j \hat{u}_i + \nabla_i \hat{u}_j - \frac{2}{3} \delta_{ij} \operatorname{div}(\hat{u}) \right) \left(\nabla_j v_i + \nabla_i v_j - \frac{2}{3} \delta_{ij} \operatorname{div}(v) \right) \right\rangle \quad (2.36c)$$

Substituting (2.36c) back to the (2.35), one can see, that by rearranging terms in the volume integral it is possible to maintain symmetry between the test and trial functions.

The weak formulation can be alternatively written in matrix form:

$$\mathbf{A} \mathbf{q}_k = s_k \mathbf{B} \mathbf{q}_k \quad (2.37)$$

Here \mathbf{A}, \mathbf{B} are the matrix representation of the left and right hand side differential operators in (2.32), \mathbf{q}_k is the state vector $(\hat{\rho}, \hat{u})$, i.e. a natural mode of the system, and s_k is the k -th eigenvalue.

2.4.3 Boundary conditions

Since the acoustics is decoupled from the mean flow, we will call inlet and outlet boundaries *free* boundaries, while the *slip* and *noslip* boundaries still have the same meaning as for the mean flow problem. Then, boundary conditions for two state variables - density and velocity perturbations ρ and u , can be written as:

$$\hat{\sigma}_{ij} n_j = 0 \quad \text{on } \Gamma_{free}, \quad (2.38a)$$

$$\hat{u}_i = 0 \quad \text{on } \Gamma_{nsl}, \quad (2.38b)$$

$$\hat{u}_i n_i = 0 \quad \text{on } \Gamma_{sl} \quad (2.38c)$$

The free boundary condition reads as zero stress on the inlet and outlet boundaries, and in the limit of zero viscosity $\nu \rightarrow 0$ it acts like a pressure (density) node.

Additionally, the presence of a slip boundary imposes the symmetry of the system. Then, every variable implies to be either an even or an odd function. In case of the normal velocity, u_n , it is odd as a result of the $u_i n_i = 0$ boundary condition. Then

it is clearly seen (e.g. from the continuity equation), that two other variables, ρ and u_τ must be even with respect to the normal symmetry. This gives us an additional boundary condition $\frac{\partial}{\partial n}u_\tau = 0$ on the symmetry plane.

Now, we can apply these boundary conditions to the weak formulation by introducing different boundary terms. Moreover, it becomes clear how to make the full weak form symmetric and still consistent with the strong form.

- Free boundary, Γ_{free}

First, free boundary models an open end; thus, a zero force boundary condition is considered. This yields:

$$\{v_i n_j \hat{\sigma}_{ij}\}_{\Gamma_{free}} = 0 \quad (2.39)$$

A possible way to enforce the zero force boundary condition is to impose it weakly by introducing a penalty boundary term [33], [10]. We add a symmetric term consistent with the primal formulation, such that the boundary integral over the free surface becomes

$$\frac{\beta}{h} \{ \sigma_{ij} n_j, \sigma_{ik}^\dagger n_k \}_{\Gamma_{free}} \quad (2.40)$$

Here β is a constant coefficient, and h is the triangulation cells size; the "daggered" stress tensor takes test functions as variables: $\sigma_{ik}^\dagger = \sigma_{ik}(w, v)$. The updated form of the boundary term is consistent with the initial problem, since $\sigma_{ij} n_j$ vanishes on Γ_{free} .

- No slip boundary, Γ_{nsl}

Second, the no slip boundary represents a rigid wall with no flow through it, so the velocity is zero at Γ_{nsl} and no restriction on density is applied. Even if the no slip boundary is curved, i.e. if the normal and tangential directions depend on the position on the boundary, the Dirichlet boundary condition can be easily applied and thus the test function can be set to zero on Γ_{nsl} . Note, that the boundary term in (2.35) is linear on v_i thus it vanishes.

- Slip boundary, Γ_{sl}

Third, the slip or symmetry boundary implies that there is no normal flow, but the tangential velocity is not specified. The slip boundary in viscous flows usually appears as a plane of symmetry, which is a line in 2D or a plane surface in 3D,

thus the Dirichlet boundary condition should be generally easy to implement. In other words, the normal velocity should vanish $u_n = 0$ as well as the normal test function can be set to zero $v_n = 0$. Assuming the surface normal being constant along the slip boundary, the surface integral becomes:

$$\begin{aligned} \{v_i \sigma_{ij} n_j\}_{\Gamma_{sl}} &= \{v_n n_i \sigma_{ij} n_j + v_\tau \tau_i \sigma_{ij} n_j\}_{\Gamma_{sl}} = \\ & \left\{ v_\tau \nu \left(\frac{\partial u_\tau}{\partial n} + \frac{\partial u_n}{\partial \tau} \right) \right\}_{\Gamma_{sl}} = 0 \end{aligned} \quad (2.41)$$

The first term vanishes due to the symmetry of the slip plane, and the second term is zero since the normal velocity component is constant in the tangent direction.

- Robin (compliant) boundary

Finally, the last boundary type to be presented is a mixed Robin boundary, or a compliant boundary. Previous boundaries were defined by either Dirichlet or Neumann type of boundary conditions. Furthermore, we can assume a mixed case or equivalently a boundary condition which relates the components of the state vector $\hat{\mathbf{q}}$ to each other; or, a value to its gradient. The velocity Robin boundary condition generally appears in the following form:

$$\frac{\partial u}{\partial n} = \frac{1}{\varepsilon}(u - u_0) + f \quad \text{on } \Gamma_{Rob}$$

As the parameter ε approaches two limit cases, $\varepsilon \rightarrow 0$ or $\varepsilon \rightarrow \infty$, the Robin boundary condition turns into a inhomogeneous Dirichlet or Neumann boundary condition, respectively. The quantities of u_0 and f then play role of prescribed velocity or velocity gradient at the boundary. Boundary condition becomes homogeneous when u_0 or f are zero.

Following [18], it is possible to extend the Nitsche approach for imposing Dirichlet boundary condition [33] to broader range of boundary types with $\varepsilon \geq 0$. The final weak formulation is consistent, symmetric and successfully compared to the traditional techniques. We refer to [18] for the detailed derivation of the general method, and the following section will consider the particular case of the Robin condition.

2.4.4 Compliant boundary

We consider the following problem: the domain now acts as a solid structure which boundaries are not fixed and can displace, reacting to the flow. This is a fluid-structure interaction (FSI) problem, and the modeled geometry and thus the computational domain may change as a result of boundary displacement. When the displacement is big enough to actually affect the mean flow, computational meshes and structure position should be moved. A number of methods describing the motion of fluid particles and mesh nodes exists, for instance the Arbitrary-Lagrange-Eulerian (ALE) approach [7]. Moving boundary condition prescribes equality of the flow and solid surface quantities, namely kinematic and dynamic conditions. First, as soon as the surface is compliant (in contrast to permeable), the continuity of displacements and velocities is required; second, the stresses in the fluid and the body should be the same [9]. These conditions couple the fluid-structure system.

Moreover, one can consider a FSI problem when boundaries are compliant, but surface deformation is tiny in comparison to the domain's size. This is the case of the inkjet printer chamber, whose height is in order of $100 \mu\text{m}$ and the boundary displacement is less than 100 nm . Then the relative displacement is lower than 10^{-3} and modelling this phenomena as a full FSI problem with the mesh movement is excessive. However, the flow can differ from those obtained with rigid slip or no slip boundary, especially for the oscillating acoustic quantities. This leads us to the idea of treating the compliant boundary in a more suitable way: with no actual domain and mesh deformation but taking into account the nature of the solid-fluid interaction on this boundary type.

The Robin boundary can describe a boundary which act like a moving membrane, reacting to the perturbations in the flow. The acoustic compliant boundary condition links the flow density (or pressure) and velocity at a certain surface point and a complex boundary impedance Z is a function which relates the normal velocity component to pressure [28]:

$$u_i n_i = -\frac{P}{Z} \quad (2.42)$$

Furthermore, we should extend this definition for the viscous acoustic problem. Recalling the idea of the impedance concept, "impedance denotes originally the ratio between a force amplitude and a velocity amplitude" [35]. Now, a force is represented not only by pressure, but also by viscous stress tensor. Then, the impedance-based relation becomes:

$$Zu_i = \sigma_{ij}n_j = (-P\delta_{ij} + \tau_{ij})n_j \quad (2.43)$$

We would neither restrict the velocity to be zero in the tangential direction, nor allow only normal displacements of the compliant boundary. Boundary impedance describes the physical properties of the boundary, such as stiffness, elasticity, thickness and others. Usually, the impedance value is known for harmonic motion with a given frequency, making the boundary condition frequency dependent: $Z = Z(s)$. As discussed before, both acoustic pressure and velocity are considered to be proportional to $(\tilde{P}, \tilde{u}) \sim e^{st}$ thus they can become out of phase due to the complex impedance boundary condition.

To apply the compliant boundary condition to viscous acoustic flow, we need to rearrange some terms in (2.43). First, performing low Mach number expansion of the impedance expression and nondimensionalizing it, we obtain an equation of the velocity and density fluctuations coupled through the dimensionless acoustic impedance, $\hat{Z} = \frac{Z}{\rho^b c_s^b}$. Second, the pressure fluctuation is substituted with density. Summing up:

$$\hat{Z}\hat{u}_i = \hat{\sigma}_{ij}n_j \quad \text{on } \Gamma_{com} \quad (2.44)$$

Now, we can derive boundary integrals of the weak problem on the compliant boundary. The boundary relation (2.44) can now be inserted into the weak form.

$$\{v_i n_j \hat{\sigma}_{ij}\}_{\Gamma_{com}} = \{Zv_i u_i\}_{\Gamma_{com}} \quad (2.45)$$

The boundary integral is symmetric; for the same reason as we did in the free boundary case, additional penalty term should be added to impose compliant boundary condition. Consequently, the compliant boundary integral becomes:

$$\{\hat{Z}v_i u_i\}_{\Gamma_{com}} + \frac{\beta}{h} \{Zu_i - \hat{\sigma}_{ij}n_j, Zv_i - \hat{\sigma}_{ij}^\dagger n_j\}_{\Gamma_{com}} \quad (2.46)$$

The initial acoustic problem is an eigenvalue problem, and previously the boundary terms were independent of s . Both terms in (2.46) is proportional to $\hat{Z}(s)$, so the impedance needs to be moved to the right hand side of the weak form. But then the problem becomes nonlinear on s , which requires to introduce some complication to the calculation routine. While this is not preferable, we assume \hat{Z} to be fixed and only rearrange the term directly dependent on s . We solve the simplified eigenvalue problem iteratively, substituting the complex frequency into the known impedance

function until the convergence criteria is reached. The algorithm for the direct and adjoint problems will be discussed separately.

Finally, two limit cases should be discussed. Compliant boundary condition is in close relation to both free and no slip conditions, which is clearly seen from (2.44). As $\hat{Z} \rightarrow 0$, the compliant boundary turns into the free surface, i.e. $n_j \hat{\sigma}_{ij} \rightarrow 0$. The boundary integral (2.46) approaches the free boundary term as well. If the impedance amplitude is high, $\hat{Z} \rightarrow \infty$, we can expect no slip behavior, and the terms proportional to \hat{Z} in (2.46) dominate, weakly imposing Dirichlet boundary condition on Γ_{com} by penalty formulation. The concept of one universal parameter, \hat{Z} in this case, which describes each of the existing boundary types with only one quantity, is quite convenient, since the development of a numerical solver becomes more generalized in comparison to boundaries with different physics behind.

Chapter 3

Adjoint based shape optimization

Modern engineering problems in aircraft design, turbomachinery, or internal flows focus on systems optimization, and shape optimization in particular, maximizing or minimizing objective function aiming to increase performance or stability. Adjoint-based optimal control methods [4] provide us with information of the system's sensitivity with respect to given parameters, for instance a channel's shape or the fluid suction rate, without additional costly computation of the system state.

We start with an introduction to shape calculus and one-dimensional examples of adjoint-based parameter optimization for unsteady Burgers equation and shape optimization for Helmholtz equation stability. Then, we follow [38], [3] and discuss viscous dissipation minimization in incompressible steady Navier–Stokes equation. Furthermore, we extend the problem to unsteady case, in particular for time-periodic flows. While we only consider time averaged viscous dissipation as an objective function, one can refer to [11] for unsteady viscous dissipation minimization and to [12] for deviation from a target velocity, drag and vorticity in incompressible viscous flows. A comprehensive overview of discrete time-dependent direct and adjoint formulation is given in [43]. An optimal control studies of drag and lift optimization for unsteady inviscid compressible flow are given in [30] and in [29], [31] for viscous compressible flow. Another application of optimal control of boundary layer flows is presented in [36]. Finally, worth mentioning adjoint-based optimization for stability of incompressible flows: investigation of vortex shedding suppression around a cylinder is given by [15], and stabilization of positive (unstable) eigenvalues via shape optimization is discussed in [32], [3].

In the last section, we present a shape optimization approach to control eigenvalues of viscous acoustic problem with compliant boundaries. This boundary condition

relates surface stress and velocity, which can be useful for modelling boundaries which are deformed by fluctuations inside the flow.

Here and later we use the following labels for scalar products:

$$\langle \cdot, \cdot \rangle = \int_{\Omega} dx (\cdot, \cdot), \quad (3.1a)$$

$$\{ \cdot, \cdot \} = \int_{\partial\Omega} d\Gamma \int_T dt (\cdot, \cdot), \quad (3.1b)$$

$$[\cdot, \cdot] = \int_{\Omega} dx \int_T dt (\cdot, \cdot) \quad (3.1c)$$

3.1 Introduction to shape calculus

We aim to study the shape optimization problem for two systems: incompressible Navier–Stokes equation and spectral viscous acoustic problem, derived in the previous chapter. Given a cost function $J(u)$, we are interested in the objective gradient with respect to the change in shape Ω , subject to the problem constraints. Here we briefly formulate the basics of shape calculus, and refer to [38] for more comprehensive review.

We call the unperturbed domain $\Omega = \Omega_0$. Consider a family of mappings

$$T_{\xi} : (\xi, x) \rightarrow T_{\xi}(x)$$

Here ξ denotes the displacement amplitude. Then the domain deformation reads as

$$\Omega_{\xi} \equiv T_{\xi}(\Omega_0) \quad (3.2)$$

The mapping operator $T_{\xi}(x)$ can be presented as a sum of identity operator \mathbf{I} and a displacement operator \mathbf{V} (also known as the speed method):

$$T_{\xi}(x) = (\mathbf{I} + \xi\mathbf{V})x = x + \xi V(x) \quad (3.3)$$

It denotes, that for $x \in \Omega$ the material derivative is defined by

$$\frac{dx}{d\xi} \equiv V(\xi, x), \quad x(0) = x_{\Omega_0} \quad (3.4)$$

In general, the gradient of the domain cost function $J(u, \Omega)$ is the object of interest:

$$dJ(\Omega)[V] = \lim_{\xi \rightarrow 0} \frac{J(u_{\xi}, \Omega_{\xi}) - J(u_0, \Omega_0)}{\xi} \quad (3.5)$$

Here $[V]$ implies the differentiation with respect to the shape perturbation (3.3), and notation ${}_{\xi}$ corresponds to the shifted boundary point or the solution in the changed domain.

Consider a function q defined as $q = q_b$ on the unperturbed boundary $\partial\Omega_0$, not dependent on surface normal. This essentially represents a Dirichlet boundary condition. We can present the full variation (or the material derivative) $dq[V]$ as a sum of local and spatial derivatives:

$$dq[V](x) = \left. \frac{d}{d\xi} \right|_{\xi=0} q_{\xi}(x_{\xi}) = \left. \frac{\partial}{\partial \xi} \right|_{\xi=0} q_{\xi} + \left. \frac{\partial q}{\partial x} \right|_{\xi=0} \frac{dx_{\xi}}{d\xi} = dq_b[V](x) \quad (3.6)$$

According to (3.4), the total derivative becomes:

$$dq[V](x) = q'[V] + (V, \nabla)q = dq_b[V](x) \quad (3.7)$$

In the case where the displacement field V is normal to the surface $V = (V, n)n$, the total derivative yields

$$dq[V](x) = q'[V] + (V, n) \frac{\partial q}{\partial n} = dq_b[V](x) \quad (3.8)$$

3.2 Pedagogical one-dimensional optimization

To start with, we consider two one-dimensional optimization problems: parameter-based unsteady Burgers equation, and Helmholtz equation with adjustable shape. These examples are aimed to give an insight into construction of adjoint systems and explain how to obtain cost function gradient with respect to different changes in the initial problem.

3.2.1 Burgers equation: sensitivity to control parameters

Burgers equation (3.9) is a nonlinear partial differential equation describing one-dimensional viscous fluid. We consider it to be defined in closed spatial domain $x \in [A, B]$ and for time interval $t \in [0, T]$.

$$u_t + uu_x - \nu u_{xx} = 0 \quad (3.9)$$

Initial condition $u(x, 0)$ is given, as well as two Dirichlet boundary conditions:

$$u(x, 0) = u_0(x), \quad (3.10a)$$

$$u(A, t) = f(t), \quad (3.10b)$$

$$u(B, t) = 1. \quad (3.10c)$$

Here the left boundary condition, $f(t)$, will act as a control parameter. We would like to optimize it in order to minimize a cost function, for instance, time-averaged viscous dissipation:

$$\mathcal{J} = \left[\nu \left(\frac{\partial u}{\partial x} \right)^2 \right] \quad (3.11)$$

Following [4], in this example we will treat initial and boundary conditions (3.10) as given constraints, i.e. in the same way as the Burgers equation. Another approach, which leads to the same result, is to apply given boundary conditions after the augmented cost function is formed.

The first step is to form the Lagrangian of the system, by adding all state equations multiplied by Lagrange variables to the cost function. This gives:

$$\mathcal{L} = \mathcal{J} - [\lambda, u_t + uu_x - \nu u_{xx}] - \quad (3.12a)$$

$$- \langle b, u(x, 0) - u_0 \rangle - \{C_\alpha, u(A, t) - f(t)\} - \{C_\beta, u(B, t) - 1\} \quad (3.12b)$$

Here λ is an Lagrange state multiplier, b and C_α, C_β are Lagrange multipliers for initial and boundary conditions, respectively. One can see, that partial derivatives of \mathcal{L} with respect to λ produce initial state equation, and initial and boundary equations while differentiation with respect to b, C_α, C_β . To construct the adjoint operator, we integrate the differential form in (3.12a) by parts and apply the divergence theorem, which results in:

$$\mathcal{L} = \mathcal{J} - \left[-\lambda_t - \frac{1}{2}u\lambda_x - \nu\lambda_{xx}, u \right] - \quad (3.13a)$$

$$- \langle \lambda, u \rangle_0^T - \left\{ \frac{1}{2}\lambda u - \nu\lambda_x, u \right\}_A^B + \{ \nu\lambda, u_x \}_A^B - \quad (3.13b)$$

$$- \langle b, u(x, 0) - u_0 \rangle - \{C_\alpha, u(A, t) - f(t)\} - \{C_\beta, u(B, t) - 1\} \quad (3.13c)$$

Now, the total variation of the Lagrangian $\delta\mathcal{L}$ can be written as:

$$0 = \delta\mathcal{L} = \delta\mathcal{J} + [\lambda_t + u\lambda_x + \nu\lambda_{xx}, \delta u] - \quad (3.14a)$$

$$- \langle \lambda(x, T), \delta u(x, T) \rangle + \langle \lambda(x, 0), \delta u(x, 0) \rangle - \quad (3.14b)$$

$$- \{ \lambda u - \nu\lambda_x, \delta u \}_A^B + \{ \nu\lambda, (\delta u)_x \}_A^B - \quad (3.14c)$$

$$- \langle b, \delta u(x, 0) \rangle - \{C_\alpha, \delta u(A, t)\} - \{C_\beta, \delta u(B, t)\} \quad (3.14d)$$

Unspecified variation of the cost function, $\delta\mathcal{J}$, is:

$$\delta\mathcal{J} = [-2\nu u_{xx}, \delta u] + \{2\nu u_x, \delta u\}_A^B \quad (3.15)$$

Finally, gathering terms with the same variation quantity, extracts the adjoint set of equations. The $[\cdot, \delta u]$ terms give the adjoint state equation:

$$\lambda_t + u\lambda_x + \nu\lambda_{xx} = 2\nu u_{xx} \quad (3.16)$$

Worth mentioning that despite this equation is quite similar to the original Burgers equation - it has temporal derivative, convective, and a viscous term, it is linear on λ , and has a source term. Moreover, viscosity has a different sign in comparison to the direct problem, thus the adjoint problem will be well-posed only propagating back in time, starting with 'initial data' at the final time $t = T$ [13]. This means, that integration in time should follow the direct solution backwards.

Gathering the rest terms provides the necessary adjoint boundary and initial conditions:

$$\delta u(x, 0) : \lambda - b = 0 \quad \Rightarrow \quad b = \lambda(x, 0), \quad (3.17a)$$

$$\delta u(x, T) : \lambda = 0 \quad \Rightarrow \quad \lambda(x, T) = 0, \quad (3.17b)$$

$$\delta u_x(A, t) : \nu \lambda = 0 \quad \Rightarrow \quad \lambda(A, t) = 0, \quad (3.17c)$$

$$\delta u_x(B, t) : \nu \lambda = 0 \quad \Rightarrow \quad \lambda(B, t) = 0, \quad (3.17d)$$

$$\delta u(A, t) : 2\nu u_x - \lambda u - \nu \lambda_x + C_\alpha = 0, \quad (3.17e)$$

$$\delta u(B, t) : 2\nu u_x - \lambda u - \nu \lambda_x - C_\beta = 0 \quad (3.17f)$$

The first two conditions (3.17a) and (3.17b) are the sensitivities to the initial condition $u(x, 0) = u_0$ and the adjoint initial condition, which says that $\lambda(x, T) = 0$; the following two are the adjoint boundary conditions, and the last two give us the values of C_α, C_β at $x = A$ and $x = B$, respectively.

Finally, from (3.13) it is clear, that the sensitivity with respect to the boundary condition $u(A, t) = f(t)$ equals to:

$$\frac{\partial \mathcal{L}}{\partial f} \delta f = \{C_\alpha, \delta f(t)\} \quad (3.18)$$

And consequently, the gradient of the cost function with respect to $f(t)$ becomes:

$$d\mathcal{J}[f] = \{C_\alpha\} = \{-2\nu u_x(A, t) + \nu \lambda_x(A, t)\} \quad (3.19)$$

3.2.2 Shape optimization of linear acoustic problem

Now we consider the one-dimensional wave equation in frequency domain, or the Helmholtz equation:

$$P_{xx} - s^2 P = 0 \quad (3.20)$$

This is a spectral problem, where P_k and s_k represent a k -th eigenfunction (or natural mode) and an eigenvalue of the given system. The general solution can be written as: $P_k = a_k e^{s_k x} + b_k e^{-s_k x}$, where a_k, b_k are some constants subject to boundary conditions.

We aim to perform shape optimization to minimize eigenvalues of the problem; namely, since the problem is 1D, we will find the derivative of the eigenvalue with respect to the position of the left boundary. Without loss of generality, let the initial domain be $x \in [0, 1]$, and let us call V the boundary displacement field at $x = 0$, such that the deformed domain is $x \in [tV, 1]$. Here t is a parameter which governs the amplitude of the displacement. Additionally, we can recast the cost function to become $\mathcal{J} = \sigma = s^2$.

The augmented cost function for the problem is defined by:

$$\mathcal{L} = \mathcal{J} + \langle \lambda, P_{xx} - \sigma P \rangle \quad (3.21)$$

Note, that we can construct the Lagrangian without knowing the boundary conditions; in contrast to the previous section, we will apply boundary conditions after the Lagrangian variation is obtained.

Integrating by parts and taking the variation of the augmented cost function (3.21) leads to:

$$0 = \delta \mathcal{L} = \delta \sigma + \langle \lambda_{xx} - \sigma \lambda, \delta P \rangle - \delta \sigma \langle \lambda, P \rangle - \quad (3.22a)$$

$$- (\lambda_x, \delta P)|_0^1 + (\lambda, \delta P_x)|_0^1 \quad (3.22b)$$

We can extract two relevant equations from this expression: first, gathering the terms of $\langle \cdot, \delta P \rangle$ and the terms proportional to $\delta \sigma$. These yield:

$$\delta P : \quad \lambda_{xx} - \sigma \lambda = 0, \quad (3.23a)$$

$$\delta \sigma : \quad 1 - \langle \lambda, P \rangle = 0. \quad (3.23b)$$

The first equation is a differential equation of the adjoint state; the second one is a normalization condition.

Now, we have two boundary terms left, and further derivation of the adjoint boundary condition will depend on the choice of the direct formulation. Here we

consider three different cases: dual Dirichlet boundary conditions, dual Neumann boundaries, and a Dirichlet plus a Robin boundary conditions.

Case 1. Dual Dirichlet boundary conditions.

Let us fix the boundary values $P(0) = P(1) = 0$, therefore the variation δP vanishes on the boundaries: $\delta P(0) = \delta P(1) = 0$. This leads to the following representation of the Lagrangian variation:

$$\delta\mathcal{L} = (\lambda, \delta P_x)|_0^1 = 0 \quad (3.24)$$

Remaining terms are proportional to the unknown δP_x thus vanish only if $\lambda(0) = \lambda(1) = 0$, which provides us with the necessary boundary conditions. The problem then becomes self-adjoint, since both the state equation and the boundary conditions are the same for the direct and the adjoint state.

Case 2. Dual Neumann boundary conditions.

Almost the same results can be obtained while considering two Neumann boundary conditions: $P_x(0) = P_x(1) = 0$, except that now another boundary term disappears leaving us with:

$$\delta\mathcal{L} = -(\lambda_x, \delta P)|_0^1 = 0 \quad (3.25)$$

Therefore we should impose two homogeneous Neumann boundary conditions on λ in order to eliminate unknown variations of δP . As a consequence, the problem is still self-adjoint with $\lambda_x(0) = \lambda_x(1) = 0$.

Case 3. Dirichlet and Robin boundary conditions.

Finally, let us introduce a mixed boundary condition at $x = 0$ and the Dirichlet at $x = 1$. Namely, $kP(0) - P_x(0) = 0$ and $P(1) = 0$, where k is some given constant. First, the boundary term proportional to $\delta P(1)$ is zero, and the second boundary term at $x = 1$ can be zero only if $\lambda(1) = 0$. Then, the remaining expression equals to:

$$\delta\mathcal{L} = (\lambda_x(0), \delta P(0)) - (\lambda(0), \delta P_x(0)) = 0 \quad (3.26)$$

The variation of the Robin boundary condition allows us to express $\delta P(0)$ or $\delta P_x(0)$ through each other, i.e. $k\delta P(0) = \delta P_x(0)$ and apply this to the boundary terms:

$$\delta\mathcal{L} = (\lambda_x(0), \delta P(0)) - (\lambda(0), k\delta P(0)) = (\lambda_x(0) - k\lambda(0), \delta P(0)) = 0 \quad (3.27)$$

This gives us the Robin boundary condition on λ , and as we can see, the direct and the adjoint problems are equivalent as well as in the previous cases. These results can be reformulated as follows: the problem (3.20) with the squared eigenvalue as the objective function is self-adjoint, and in order to obtain the adjoint field λ one should apply the normalization condition (3.23b).

Following [38], but with the simplification to 1D case, we can present the full variation (or the material derivative) as a sum of local and spatial derivatives:

$$dP[V](x) = P'[V] + VP_x \quad (3.28)$$

Furthermore, the material derivative of the spatial derivative P_x can be written as:

$$dP_x[V](x) = (P'[V])' + VP_{xx} \quad (3.29)$$

Now, to cover all three cases at once, let us derive the shape derivative of the objective function for Case 3. First, from the Robin boundary condition and using the expressions for the material derivatives:

$$d(P_x - kP) = 0 \quad \Rightarrow \quad (P'[V])' = kP'[V] + kVP_x - VP_{xx} \quad (3.30)$$

And the Lagrangian shape derivative

$$\mathcal{L}'[V] = (\lambda_x, P'[V])_{x=0} - (\lambda, (P'[V])')_{x=0} = \quad (3.31a)$$

$$(\lambda_x - k\lambda, P'[V])_{x=0} - (\lambda, kVP_x - VP_{xx})_{x=0} \quad (3.31b)$$

Since the system is self-adjoint, we can use $P(x)$ instead of $\lambda(x)$ (keeping in mind the normalization condition), the first bracket in (3.31b) is zero due to the boundary condition $\lambda_x - k\lambda = 0$; and the shape derivative finally becomes:

$$d\sigma[V] = V (PP_{xx} - kPP_x)_{x=0} = V (PP_{xx} - P_x^2)_{x=0} \quad (3.32)$$

Summing up, once the solution of the spectral problem (3.20) is obtained, to calculate the shape derivative of the cost function $\mathcal{J} = s^2$ with respect to shape one needs to normalize the eigenfunction such way that $1 = \langle P, P \rangle$, and then the desired gradient equals to (3.32). Note, that it doesn't depend on k .

3.3 Adjoints for incompressible Navier–Stokes equation

This section reviews the adjoint state derivation for incompressible Navier–Stokes equation and formulates shape derivatives for viscous dissipation as the cost function. We follow [3] for general steady adjoint formulation and [38] to construct the shape derivative in Hadamard form.

3.3.1 Governing equations

Let us recall the direct unsteady Navier–Stokes problem first. The momentum balance and the divergence constraint read

$$\mathbb{N}_i(u, P) = \frac{\partial u_i}{\partial t} + (u_j \nabla_j) u_i + \nabla_i P - \nu \Delta u_i = 0, \quad (3.33a)$$

$$\mathbb{P}(u, P) = \operatorname{div}(u) = 0 \quad (3.33b)$$

We choose viscous dissipation as the objective function:

$$\mathcal{J} = \nu \int_T \int_{\Omega} (\nabla_i u_j)^2 \, d\mathbf{x} dt = [(\nabla_i u_j)^2] \quad (3.34)$$

Constrained optimization problems requires two Lagrange variables, vector function λ_i , and scalar function λ_p . Aiming to derive the co-state equations, we start with the Lagrangian of the system:

$$\mathcal{L} = \mathcal{J} - [\lambda_i, \mathbb{N}_i(u, P)] - [\lambda_p, \mathbb{P}(u, P)] \quad (3.35)$$

Now, variations with respect to adjoint variables $\frac{\partial \mathcal{L}}{\partial \lambda}$ result in the state equations, and $\frac{\partial \mathcal{L}}{\partial \mathbf{u}}$ gives adjoint (costate) equations. We perform integration by parts, and regroup the terms:

$$\mathcal{L} = [(\nabla_i u_j)^2] - \left[\lambda_i, \frac{\partial u_i}{\partial t} + (u_j \nabla_j) u_i + \nabla_i P - \nu \Delta u_i \right] - [\lambda_p, \text{div}(u)] = \quad (3.36a)$$

$$[-\nu u_k \nabla_i^2 u_k] + \left\{ \nu u_k \frac{\partial u_k}{\partial n} \right\} - \quad (3.36b)$$

$$\left[u_i, -\frac{\partial \lambda_i}{\partial t} - u_j \nabla_j \lambda_i - \Delta \lambda_i \right] - [P, -\nabla_i \lambda_i] - \quad (3.36c)$$

$$\left\{ \lambda_i (u_j n_j u_i + n_i P) + \nu \left(u_i \frac{\partial \lambda_i}{\partial n} - \lambda_i \frac{\partial u_i}{\partial n} \right) \right\} - \langle \lambda_i(T), u_i(T) \rangle + \langle \lambda_i(0), u_i(0) \rangle - \quad (3.36d)$$

$$[u_i, -\nabla_i \lambda_p] - \{ \lambda_p u_i n_i \} \quad (3.36e)$$

Here, (3.36a) is the initial Lagrangian formulation; the volume and the surface terms related to the cost function is (3.36b); (3.36c) and (3.36d) come from the momentum equation integration by parts, and the last term (3.36e) is the velocity divergence constraint. We take the state variation of the Lagrangian and focus on the volumetric terms:

$$\frac{\partial \mathcal{L}}{\partial u_i} = 0 : \quad \frac{\partial \lambda_i}{\partial t} + u_j \nabla_j \lambda_i + u_j \nabla_i \lambda_j + \nu \Delta \lambda_i + \nabla_i \lambda_p = 2\nu \Delta u_i, \quad (3.37a)$$

$$\frac{\partial \mathcal{L}}{\partial P} = 0 : \quad \text{div}(\lambda) = 0 \quad (3.37b)$$

Equations (3.37) define the adjoint problem, subject to given boundary and initial conditions. Same as for the discussed one-dimensional Burgers equation, the time derivative and the viscous terms share sign, thus the adjoint "flow" should be considered and solved backwards in time, otherwise the problem becomes ill-posed.

The unsteady problem can be easily converted to the steady case, by setting present time derivative to zero.

3.3.2 Adjoint initial and boundary conditions

The volume integrals in the variation of (3.36) are zero due to the choice of adjoint governing equations, (3.37). In order to derive relevant adjoint boundary and initial conditions, let us notice that the following terms in the variational form are left:

$$\delta\mathcal{L} = \left\{ 2\nu\delta u_k \frac{\partial u_k}{\partial n} \right\} - \quad (3.38a)$$

$$\left\{ \lambda_i(\delta u_j n_j u_i + u_j n_j \delta u_i + n_i \delta P) + \nu \left(\delta u_i \frac{\partial \lambda_i}{\partial n} - \lambda_i \frac{\partial \delta u_i}{\partial n} \right) \right\} - \quad (3.38b)$$

$$\{ \lambda_p \delta u_i n_i \} - \langle \lambda_i(T), \delta u_i(T) \rangle + \langle \lambda_i(0), \delta u_i(0) \rangle \quad (3.38c)$$

First, the choice of the boundary conditions comes from the surface terms as follows.

- Inlet and no slip boundaries

In both cases, u_i is known thus its variation δu_i is zero. Then, the Lagrangian variation immediately yields:

$$\delta\mathcal{L}_{\Gamma_{nsl}, \Gamma_{in}} = 0 = \left\{ \lambda_i \nu \frac{\partial \delta u_i}{\partial n} \right\}_{\Gamma_{nsl}, \Gamma_{in}} \quad (3.39)$$

Therefore, the inlet and no slip adjoint boundary conditions become

$$\lambda_i = 0 \quad \text{on} \quad \Gamma_{nsl}, \Gamma_{in} \quad (3.40)$$

- Outlet boundary

Outlet boundary is stress-free, namely $-Pn_i + \nu \frac{\partial u_i}{\partial n} = 0$. Inserting the variation of this expression into (3.38), we obtain:

$$\delta\mathcal{L}_{\Gamma_{out}} = 0 = \left\{ \left(\lambda_i u_j n_j + \lambda_j u_j n_i + \nu \frac{\partial \lambda_i}{\partial n} + \lambda_p n_i - 2\nu \frac{\partial u_i}{\partial n} \right) \delta u_i \right\}_{\Gamma_{out}} \quad (3.41)$$

This provides us the outlet adjoint boundary condition

$$\lambda_i u_j n_j + \lambda_j u_j n_i + \nu \frac{\partial \lambda_i}{\partial n} + \lambda_p n_i - 2\nu \frac{\partial u_i}{\partial n} = 0 \quad \text{on} \quad \Gamma_{out} \quad (3.42)$$

Second, we require one initial condition for the adjoint problem. Since the initial condition of the direct problem $u_i(x, t = 0) = u_0(x)$ is known, its total variation is zero, and the remaining term is:

$$- \langle \lambda_i(T), \delta u_i(T) \rangle = 0 \quad (3.43)$$

Consequently, the adjoint initial condition holds at $t = T$ and reads

$$\lambda_i(x, T) = 0 \quad (3.44)$$

3.3.3 Shape derivative and Hadamard structure

Viscous dissipation shape optimization problem requires knowledge of the cost function gradient with respect to geometry deformation. Consider we are given a displacement field V on the no slip boundary, and $\mathcal{L}'[V] = d\mathcal{J}[V]$ is the quantity of interest.

First, for a general volume objective $F = \int f d\mathbf{x} \equiv [f]$, the equality holds:

$$F'[V] = \{(V, n)f\} + [f'[V]] \quad (3.45)$$

If $f \equiv 0$, which is true for the equality constraint condition, only the $[f'[V]]$ remains. Thus, the shape derivative of the Lagrangian (3.36) becomes:

$$\mathcal{L}'[V] = \{(V, n)\nu(\nabla_j u_i)^2\} + [2\nu\nabla_j u'_i[V]\nabla_j u_i] - \quad (3.46a)$$

$$\left[u'_i[V], -\frac{\partial \lambda_i}{\partial t} - u_j \nabla_j \lambda_i - u_j \nabla_i \lambda_j - \Delta \lambda_i \right] - [P'[V], -\nabla_i \lambda_i] - \quad (3.46b)$$

$$\left\{ \lambda_i(u'_j[V]n_j u_i + u_j n_j u'_i[V] + n_i P) + \nu \left(u'_i[V] \frac{\partial \lambda_i}{\partial n} - \lambda_i \frac{\partial u'_i[V]}{\partial n} \right) \right\} - \quad (3.46c)$$

$$\langle \lambda_i(T), u'_i[V](T) \rangle + \langle \lambda_i(0), u'_i[V](0) \rangle - \quad (3.46d)$$

$$[u'_i[V], -\nabla_i \lambda_p] - \{\lambda_p u'_i[V] n_i\} \quad (3.46e)$$

One can notice, that all the volume terms [...] are zero due to the choice of adjoint state equations. Then, since we consider the displacement to be non-zero only on no slip boundary, we apply appropriate adjoint boundary condition $\lambda_i = 0$ and the shape derivative becomes:

$$\mathcal{L}'[V] = \{(V, n)\nu(\nabla_j u_i)^2\} - \left\{ \nu \left(u'_i[V] \frac{\partial \lambda_i}{\partial n} - \lambda_i[V] \frac{\partial u_i}{\partial n} \right) \right\} - \{\lambda_p u'_i[V] n_i\} + \langle \lambda_i(0), u'_i[V](0) \rangle \quad (3.47)$$

The shape sensitivity term $u'_i[V]$ immediately comes from the boundary condition derivative:

$$du_i = 0 = u'_i[V] + (V, n) \frac{\partial u_i}{\partial n} \quad \text{on } \Gamma_{nsl} \quad (3.48)$$

On no slip boundary $u_i = 0$ and therefore $\partial u_i / \partial \tau = 0$. From $\text{div}(u) = 0$ it comes, that $n_i \partial u_i / \partial n = 0$, and the term proportional to λ_p vanishes. Substituting the shape derivative (3.48), we obtain:

$$dJ[V] = \mathcal{L}'[V] = \left\{ (V, n) \nu \frac{\partial u_i}{\partial n} \left(\frac{\partial \lambda_i}{\partial n} - \frac{\partial u_i}{\partial n} \right) \right\} + \langle \lambda_i(0), u'_i[V](0) \rangle \quad (3.49)$$

Here, the surface term in Hadamard form denotes the general shape derivative of steady incompressible Navier–Stokes equation for viscous dissipation; and the volumetric term at $t = 0$ comes from the unsteady formulation. Note, that the second term is not in Hadamard form and should be integrated over the whole domain. To explain the physics behind this, we should consider two different geometries and the way we choose the initial flow state. This might be the case of, by way of illustration, a flow with a oscillating inlet velocity profile. One can propose starting the unsteady simulation from a steady solution in order to avoid the irrelevant transition region. However, then $u_i(t = 0)$ will depend on the choice of geometry and $u'_i[V](t = 0)$ doesn't disappear. To avoid calculating the volumetric state sensitivity, we propose setting initial condition to zero everywhere. Then, if we aim to minimize the objective function over a semi-steady oscillation period, or a large number of flow periods is being simulated, the presence of the transition region can be neglected since its relative contribution limits to zero.

3.3.4 Euler method for time-dependent adjoint system

Time integration of (3.37) requires knowledge about the flow state $u_i(x, t)$ at each time step. It means, that one needs to

1. Solve the direct equations (3.33) for $t \in [0, T]$,
2. Store flow states for each time step in t ,
3. Use the corresponding flow state while solving the time-dependent adjoint problem

The adjoint momentum equation propagates back in time and space, so we assume that all the "future" values are known, as well as the direct state. We perform time discretization (upper indices denote time step number):

$$-\frac{\lambda_i^n - \lambda_i^{n+1}}{\Delta t} + \mathbb{L}_i(\mathbf{u}^n) \lambda^n = 2\nu \Delta u_i^n \quad (3.50)$$

Here $\mathbb{L}_i(\mathbf{u}^n)$ is the steady adjoint differential operator acting on (λ_i, λ_p) . The unknown λ_i^n is the solution of the following linear equation:

$$\left(-\frac{1}{\Delta t} + \mathbb{L}_i(\mathbf{u}^n)\right) \lambda^n = 2\nu \Delta u_i^n - \frac{\lambda_i^{n+1}}{\Delta t} \quad (3.51)$$

Finally, for a uniform partitioning of the time interval $t \rightarrow (t_0, t_1, \dots, t_N)$ with the time step Δt , the time discrete shape derivative can be calculated as

$$dJ[V] = \sum_{n=0}^{T/\Delta t} \Delta t \left\{ (V, n) \nu \frac{\partial u_i^n}{\partial n} \left(\frac{\partial \lambda_i^n}{\partial n} - \frac{\partial u_i^n}{\partial n} \right) \right\} \quad (3.52)$$

3.4 Adjoint viscous acoustic problem

In this section we derive and discuss the adjoint formulation of the viscous acoustic problem. First, we formulate the governing equations of the adjoint state; second, the adjoint boundary conditions are presented, and third, the shape derivative in the Hadamard form is constructed.

3.4.1 Governing equations

Let us recall the formulation of the direct problem, (2.32). We will use the following form of the acoustic continuity and momentum conservation equations in the frequency domain:

$$s\hat{\rho} + \operatorname{div}(\hat{u}) = 0, \quad (3.53a)$$

$$s\hat{u}_i - \nabla_j \hat{\sigma}_{ij} = 0. \quad (3.53b)$$

We aim to control the natural frequencies of the system, therefore s is the objective function $\mathcal{J} = s$. We obtain the augmented cost function by multiplying the first equation in (3.53a) by a scalar function $-w$ and the second equation by a vector function v_i . Now, the Lagrangian can be written as:

$$\mathcal{L} = \mathcal{J} - \langle -w, s\hat{\rho} + \operatorname{div}(\hat{u}) \rangle - \langle v_i, s\hat{u}_i - \nabla_j \hat{\sigma}_{ij} \rangle \quad (3.54)$$

We integrate the volume integrals by parts, and regroup the terms:

$$\mathcal{L} = \langle sw + \operatorname{div}(v), \hat{\rho} \rangle - \langle sv_i - \nabla_j \sigma_{ij}^\dagger, \hat{u}_i \rangle + \{v_i, \hat{\sigma}_{ij} n_j\} - \{\sigma_{ij}^\dagger n_j, \hat{u}_i\} \quad (3.55)$$

As stated previously, $\langle \cdot, \cdot \rangle$ here denotes volume integrals, while $\{\cdot, \cdot\}$ is used to describe surface integrals. We denote the stress tensor operator acting on the co-state space (w, v_i) as $\sigma_{ij}^\dagger = -w\delta_{ij} + \nu(\nabla_j v_i + \nabla_i v_j - \frac{2}{3}\delta_{ij}\operatorname{div}(v))$. Now, the variation of the Lagrangian with respect to s and $\hat{\rho}, \hat{u}_i$ results in the adjoint set of equations:

$$\delta s : \langle \hat{u}_i v_i - \rho w \rangle = 1, \quad (3.56a)$$

$$\delta \hat{\rho} : sw + \operatorname{div}(v) = 0, \quad (3.56b)$$

$$\delta \hat{u}_i : sv_i - \nabla_j \sigma_{ij}^\dagger = 0 \quad (3.56c)$$

Here, the first equation acts as a normalization condition, and the second and third equations describe the adjoint continuity and momentum conservation laws. Note, that the state and co-state equations are equal; we expect the system to be self-adjoint. To show this, let us consider the possible boundary conditions.

3.4.2 Adjoint boundary conditions

We consider three types of boundary conditions of the direct problem: no-slip boundary $\hat{u}_i = 0$, stress-free boundary $\hat{\sigma}_{ij}n_j = 0$, and compliant boundary $Z\hat{u}_i = \hat{\sigma}_{ij}n_j$. For each of the boundary types we will focus on the surface integrals in (3.55) since the volumetric terms vanish due to the choice of the adjoint state equations.

The general expression of the surface terms variation reads as:

$$\delta\mathcal{L} = \{v_i, \delta\hat{\sigma}_{ij}n_j\} - \{\sigma_{ij}^\dagger n_j, \delta\hat{u}_i\} = 0 \quad (3.57)$$

No-slip boundary

The variation of the no-slip Dirichlet boundary condition is zero, $\delta\hat{u}_i = 0$, which leaves us with the following condition:

$$\{v_i, \delta\hat{\sigma}_{ij}n_j\}_{\Gamma_{nsl}} = 0 \quad (3.58)$$

Since the stress value is not specified on the no-slip boundary, we set the adjoint velocity v_i to zero:

$$v_i = 0 \quad \text{on } \Gamma_{nsl} \quad (3.59)$$

Free boundary

On the free boundary, the stress vector is given thus its variation is zero. The Lagrangian variation then becomes

$$- \{\sigma_{ij}^\dagger n_j, \delta\hat{u}_i\}_{\Gamma_{free}} = 0 \quad (3.60)$$

In order to eliminate the unknown velocity variation on the free boundary, we choose adjoint stress to be zero as well:

$$\sigma_{ij}^\dagger n_j = 0 \quad \text{on } \Gamma_{free} \quad (3.61)$$

Compliant boundary

The compliant boundary condition couples the velocity and the stress on the surface, therefore the variation of the boundary condition is $Z\delta\hat{u}_i = \delta\hat{\sigma}_{ij}n_j$. Although the impedance value depends on the oscillation frequency $Z = Z(s)$, we assume that the variation of Z is zero, i.e. neglect that the boundary impedance is not constant. We substitute the variation expression into (3.57) to obtain

$$\{v_i, Z\delta\hat{u}_i\}_{\Gamma_{comp}} - \{\sigma_{ij}^\dagger n_j, \delta\hat{u}_i\}_{\Gamma_{comp}} = \{Zv_i - \sigma_{ij}^\dagger n_j, \delta\hat{u}_i\}_{\Gamma_{comp}} = 0 \quad (3.62)$$

The surface integral is proportional to unknown $\delta\hat{u}_i$, so the compliant adjoint boundary condition becomes

$$Zv_i = \sigma_{ij}^\dagger n_j \quad \text{on } \Gamma_{comp} \quad (3.63)$$

First, note, that all the adjoint boundary conditions are equivalent to the direct formulation. This proves that the proposed problem is self-adjoint. Second, the compliant boundary is a generalized case of the no-slip and stress-free boundaries; if Z approaches infinity, the boundary acts like a no-slip, and represents a free surface if $Z \rightarrow 0$. Consequently, once we obtain any result for the compliant boundary, it can be easily applied to all other mentioned cases without any additional effort.

Summing up, we have derived the adjoint boundary conditions for no-slip, stress-free, and compliant boundaries. It appears, that they are similar to those of the direct problem, and as soon as the adjoint governing equations coincide with the primal formulation, the problem is self-adjoint. The only step to calculate the adjoint quantities is to apply the normalization condition (3.56a).

3.4.3 Shape derivative and Hadamard structure

Let us recall the main concept of the Hadamard formula first: for a sufficiently smooth cost function, \mathcal{J} , the shape derivative $d\mathcal{J}[V]$ can be written as a surface integral of the given domain perturbation field V and a functional G . In our case, we aim to construct the gradient of the cost function (eigenvalue) by deriving the integrand G as a function of the direct and adjoint states: $G = G(\mathbf{q}, \mathbf{q}^\dagger)$. Since the problem we consider is self-adjoint, the Hadamard formula yields:

$$d\mathcal{J}[V] = \int_{\partial\Omega} (V, n)G(\mathbf{q})d\Gamma \quad (3.64)$$

As shown below, all considered boundary conditions thus shape derivatives can be translated to the single case of the compliant boundary. Using the chain rule, the material derivative of the boundary condition satisfies

$$0 = d(Z\hat{u}_i - \hat{\sigma}_{ij}n_j)[V] = \quad (3.65a)$$

$$Zd\hat{u}_i[V] - d\hat{\sigma}_{ij}[V]n_j - \hat{\sigma}_{ij}dn_j[V] \quad (3.65b)$$

Applying (3.7), the boundary derivative terms read as

$$d\hat{u}_i[V] = \hat{u}'_i[V] + (V, \nabla)\hat{u}_i, \quad (3.66a)$$

$$d\hat{\sigma}_{ij}[V] = \hat{\sigma}'_{ij}[V] + (V, \nabla)\hat{\sigma}_{ij} \quad (3.66b)$$

Specifically, for the perturbation normal to the boundary $V = (V, n)n$, the shape derivative of the normal is given by tangent gradient of the displacement, $\nabla_i^\Gamma(V, n)$ [38]. The tangent gradient is defined as gradient minus its normal component $\nabla_i^\Gamma = \nabla_i - n_i\partial_n$.

$$dn_i[V] = -\nabla_i^\Gamma(V, n) \quad (3.67)$$

The eigenvalue shape derivative of the problem (3.56) now becomes

$$d\mathcal{J}[V] = \{v_i, \hat{\sigma}'_{ij}[V]n_j\} - \{\sigma_{ij}^\dagger n_j, \hat{u}'_i[V]\} = \quad (3.68a)$$

$$\{v_i, d\hat{\sigma}_{ij}[V]n_j - (V, \nabla)\hat{\sigma}_{ij}n_j\} - \{\sigma_{ij}^\dagger n_j, d\hat{u}_i[V] - (V, \nabla)\hat{u}_i\} = \quad (3.68b)$$

$$\{v_i, Zd\hat{u}_i[V] - \hat{\sigma}_{ij}dn_j[V] - (V, \nabla)\hat{\sigma}_{ij}n_j\} - \{\sigma_{ij}^\dagger n_j, d\hat{u}_i[V] - (V, \nabla)\hat{u}_i\} = \quad (3.68c)$$

$$\{\hat{u}_i, Zd\hat{u}_i[V] - \hat{\sigma}_{ij}dn_j[V] - (V, \nabla)\hat{\sigma}_{ij}n_j\} - \{\hat{\sigma}_{ij}n_j, d\hat{u}_i[V] - (V, \nabla)\hat{u}_i\} = \quad (3.68d)$$

$$\{\hat{u}_i, -\hat{\sigma}_{ij}dn_j[V] - (V, \nabla)\hat{\sigma}_{ij}n_j\} - \{\hat{\sigma}_{ij}n_j, -(V, \nabla)\hat{u}_i\} \quad (3.68e)$$

Considering only normal boundary displacement, the shape derivative becomes

$$d\mathcal{J}[V] = \left\{ (V, n) \left(\frac{\partial \hat{u}_i}{\partial n} n_j \hat{\sigma}_{ij} - \hat{u}_i n_j \frac{\partial \hat{\sigma}_{ij}}{\partial n} \right) + \hat{u}_i \hat{\sigma}_{ij} \nabla_j^\Gamma(V, n) \right\} \quad (3.69)$$

This is still not in the Hadamard form, so we apply the surface tangential Green's formula [6] to the last term. The relation holds for a smooth vector field A and a scalar field b :

$$(A, \nabla^\Gamma)b = \kappa b(A, n) - b \operatorname{div}^\Gamma A \quad (3.70)$$

Here $\kappa = \operatorname{div}^\Gamma n$ describes the surface curvature. The transformation to the Hadamard form is given by

$$\hat{u}_i \hat{\sigma}_{ij} \nabla_j^\Gamma (V, n) = \kappa(V, n) \hat{u}_i \hat{\sigma}_{ij} n_j - (V, n) \nabla_j^\Gamma (\hat{u}_i \hat{\sigma}_{ij}) \quad (3.71)$$

Furthermore, using the definition of the tangential gradient, the relation holds:

$$\nabla_j^\Gamma (\hat{u}_i \hat{\sigma}_{ij}) + \hat{u}_i n_j \frac{\partial \hat{\sigma}_{ij}}{\partial n} = \nabla_j (\hat{u}_i \hat{\sigma}_{ij}) - \frac{\partial \hat{u}_i}{\partial n} n_j \hat{\sigma}_{ij} \quad (3.72)$$

After rearranging the terms in (3.69), the shape derivative of the system's eigenvalue becomes:

$$ds[V] = \left\{ (V, n) \left(2 \frac{\partial \hat{u}_i}{\partial n} n_j \hat{\sigma}_{ij} - \nabla_j (\hat{u}_i \hat{\sigma}_{ij}) + \kappa \hat{u}_i \hat{\sigma}_{ij} n_j \right) \right\} \quad (3.73)$$

A few comments to be made regarding the shape derivative expressions. First, two forms (3.69) and (3.73) are equivalent. Second, they do not depend on Z , thus are applicable to any considered boundary type. Third, in case \hat{u}_i or $\hat{\sigma}_{ij} n_j$ is zero, some of the terms vanish which can be useful in case of a single boundary type evaluation.

3.5 Taylor testing for adjoint gradient

The combination of the direct and adjoint problem solutions, and the expression for the shape derivative of a considered objective function allows us to calculate the change of the objective function with respect to the change of the system's parameters. For the case of shape optimization problem, we consider a number of control points governing the geometry of the system as adjustable variables. This adjoint-based approach allows to evaluate the sensitivity of the objective to the control points positions with only one calculated state, while a common finite difference approach requires knowledge of at least two close states.

Once we are satisfied with the results obtained from the direct problem, for instance, the spectrum of the acoustic problem or the base flow, it becomes necessary to verify the gradients we calculate via the finite difference and the adjoint approaches. To perform this check, one could definitely compare a few objective function values at different parameter choices. However, as we will show, sometimes it is required to apply a bit more sophisticated method, especially if your solver has not been tested yet or it is expected that the results can depend on the mesh resolution, choice of function spaces or other features of the numerical solution.

Consider a single variable objective function, $f(x)$, which values we know at $N + 1$ points x_0, x_1, \dots, x_N in our one-dimensional parameter space $x \in X$. Taylor expansion of the function around the unperturbed solution $f(x_0)$ yields:

$$f(x) = f(x_0) + \left. \frac{\partial f}{\partial x} \right|_{x=x_0} (x - x_0) + \frac{1}{2} \left. \frac{\partial^2 f}{\partial x^2} \right|_{x=x_0} (x - x_0)^2 + \mathcal{O}((x - x_0)^3) \quad (3.74)$$

The question we would like to ask is: how can we calculate the accuracy of the adjoint-based gradient $f_a(x_0)$? Without loss of generality, we will explain the Taylor test procedure for the first data point, since given the set of $x, f(x)$ and $f_a(x)$, the choice of x_0 is completely arbitrary.

We expect the difference between $f_a(x_0)$ and $\partial f/\partial x|_{x=x_0} = (f(x_k) - f(x_0))/(x_k - x_0)$ to be zero, if the shape derivative was formulated completely. Thus, it is natural to formulate a deviation function as

$$\delta f(x) = f(x) - f(x_0) - f_a(x_0)(x - x_0) = \quad (3.75a)$$

$$\left(\frac{\partial f}{\partial x} \Big|_{x=x_0} - f_a(x_0) \right) (x - x_0) + \frac{1}{2} \frac{\partial^2 f}{\partial x^2} \Big|_{x=x_0} (x - x_0)^2 + \mathcal{O}((x - x_0)^3) \quad (3.75b)$$

Using Δx instead of $x - x_0$ gives us:

$$\delta f(\Delta x) = \left(\frac{\partial f}{\partial x} \Big|_{x=x_0} - f_a(x_0) \right) \Delta x + \frac{1}{2} \frac{\partial^2 f}{\partial x^2} \Big|_{x=x_0} \Delta x^2 + \mathcal{O}(\Delta x^3) \quad (3.76)$$

If the adjoint shape gradient coincides with the finite difference gradient, and Δx is sufficiently small, the deviation function should act (at least) as parabola, i.e. having the leading term of Δx^2 or higher as $\Delta x \rightarrow 0$. Otherwise, the calculated adjoint gradient is wrong. Alternatively, one can consider the deviation as a function of Δx^2 , giving us

$$\delta f(y) = \left(\frac{\partial f}{\partial x} \Big|_{x=x_0} - f_a(x_0) \right) \sqrt{y} + \frac{1}{2} \frac{\partial^2 f}{\partial x^2} \Big|_{x=x_0} y + \mathcal{O}(y^2) \quad (3.77)$$

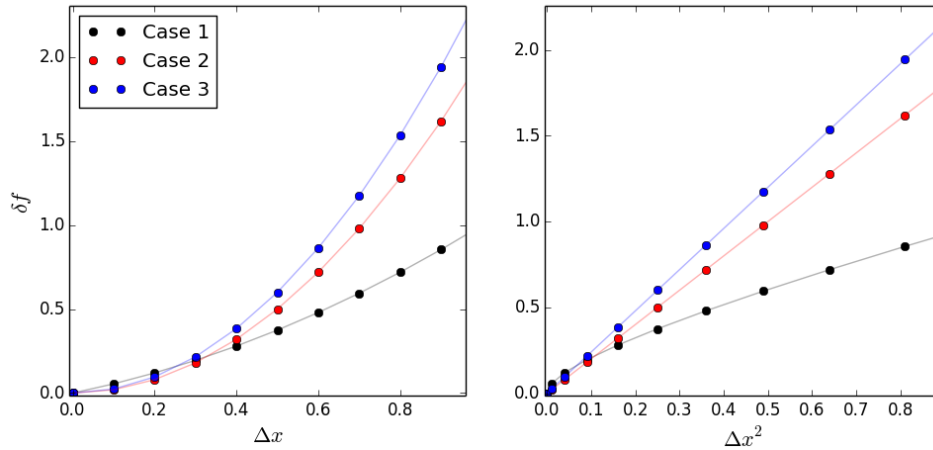


Fig. 3.1 Taylor tests of adjoint gradients for three cases: mismatching adjoint and finite difference gradients (Case 1), matching gradients (Case 2), and matching gradients with nonlinear terms dominating (Case 3).

Fig.3.1 illustrates three cases of $\delta f(\Delta x)$ and $\delta f(\Delta x^2)$ behaviour. In the first case, the linear term is non zero, which points out the discrepancy between the finite difference and adjoint based differentiation. As $\Delta x \rightarrow 0$, it acts like a straight line on the left figure and square root on the right hand side. The second case represents a correctly matching gradients, so the parabola on the left plot has zero slope at $\Delta x = 0$, and $f(\Delta x^2)$ is a straight line. A special third case occurs if second derivative of the considered function is zero, so the deviation grows faster than quadratic or linear function, which corresponds to the higher order terms coming out.

Investigation of the deviation function $\delta f(\Delta x^2)$ behaviour reduces to simple linear regression, and consequent comparison of the data set and the approximation. If the experimental data points start to bend down at some Δx^2 value, this instantly shows the presence of the gradient estimation error.

Alternatively, one can work on quadratic fitting for the $\delta f(\Delta x)$ deviation function. The advantage of this approach is that it basically provides more useful data to rely on. First, as well as in the first approach, we evaluate the deviation at $\Delta x = 0$, namely the approximated constant term. In general, it should be zero, while any noticeable difference points out that the model is incorrect. Second, the obtained linear term stands for the actual difference between finite difference and adjoint gradients. Thus, we can control how large is this difference and conclude whether we are satisfied with the obtained accuracy or not. Usually, the deviation at $\Delta x = 0$ should be in order of machine precision, and the linear term of the approximation is no more than thousandth of the adjoint gradient value.

The last thing to mention, is that in the particular shape optimization case when a new mesh is generated each time the parameter space changes, the process of re-meshing can produce a noticeable gradient error itself. In present work, we observed this, especially for tiny changes of parameters.

Chapter 4

Applications

4.1 Computational methods

We perform spatial discretization using the finite elements method for both unsteady incompressible Navier–Stokes equation and viscous acoustic eigenvalue problem. The continuous Galerkin approach was chosen for its simplicity in constructing weak forms, and for the well-known Taylor–Hood P1P2 elements for the convection-dominated mean flow solving.

Because developing and validating new solvers is extremely costly and hard, we chose the open-source finite elements computing platform FEniCS [26] for solving partial differential equations. It provides a straightforward high-level Python interface, which allows to write human-readable code. In addition, numerous scientific packages has been already implemented in Python, in particular *numpy* and *scipy* for general mathematical operations and PETSc and SLEPc for matrix operations. Inspired by previous research done in [3], especially for eigenvalue solvers optimization, we implemented complex shift to FEniCS (see Appendix C). We consider Gmsh package and its Python interface PyGmsh as the main mesh generating tool.

To fully take advantage of the finite elements and spectral solver, and mesh generating toolkit, a in-house solver has been developed [21]. It has a build-in CAD-like geometry generator, an unsteady incompressible solver and a viscous acoustic solver. To give an example of the tool, let us consider a two-dimensional rectangular 5×1 channel, and a top adjustable Bezier-parametrized boundary. We aim to calculate sensitivities of viscous dissipation and the real part of the first eigenvalue with respect to the control point position. A code snippet below shows this.

First, we load necessary libraries for elements with prescribed boundary conditions, channel geometry class, and solver classes.

```

1 from Domain import boundaryElement
2 from Domain import Channel
3 from solver import SpectralSolver_2D
4 from solver import IncSolver_2D

```

We define four boundaries as *boundaryElements*: inlet with prescribed uniform velocity profile, outlet, and two rigid boundaries. The triangulation size h is defined by the *elSize* parameter. Then, we construct a *Channel*:

```

1 InletBoundary = boundaryElement(boundaryType = ['inlet', [1.,0.]], 'box',
2                                 control points = [[0., 0.],[0., 1.]],
3                                 elSize = 0.01]
4 ComplBoundary = boundaryElement(boundaryType = ['compliant', Z=[10.,10.]], 'bezier',
5                                 control points = [[0., 1.], [2.5,1.], [5.,1.]],
6                                 elSize = 0.01]
7 OutletBoundary = boundaryElement(boundaryType = ['outlet'], 'box',
8                                 control points = [[5.,1.],[5.,0.]],
9                                 elSize = 0.01]
10 NoslipBoundary = boundaryElement(boundaryType = ['noslip'], 'box',
11                                 control points = [[5.,0.],[0.,0.]],
12                                 elSize = 0.01]
13
14 Channel = Channel(InletBoundary, ComplBoundary, OutletBoundary, NoslipBoundary)

```

Now, we create an incompressible solver, and run an unsteady simulation from $t = 0$ to $t = 1$ with time step $\Delta t = 0.01$. Then, we integrate the adjoint field and calculate the cost function gradient with respect to the given boundary:

```

1 solver_Inc = IncSolver_2D(Re = 100, Geometry, ['unsteady', 0.01, 0.0, 1.0])
2
3 solver_Inc.AdjSovle_unsteady(ComplBoundary)

```

For the spectral solver, we specify the number of eigenmodes to find, and the spectral shift:

```

1 solver_Sp = SpectralSolver_2D(Re-Cs = 1.e4, Geometry)
2
3 solver_Sp.solve(1, shiftR = 0.0, shiftIm = 1.0)
4
5 solver_Sp.dJv(ComplBoundary)

```

This allows us to calculate the desired cost functions sensitivities in less than 30 lines. The solver automatically calculates displacement field, stores the solutions, and saves the sensitivities. One can easily apply gradient-based algorithms to perform shape optimization. The gradient descent algorithm with Armijo backtracking linesearch [2] has been implemented.

4.2 Shape optimization for stability

In this chapter we present the shape optimization results for a two dimensional channel stability. The results has also been presented in [22]. Using the gradient information provided by (3.73), we can adjust the geometry and control the position of system's eigenvalues, and, for instance, decrease the real part (increase the decay rate) of the first natural mode of the system. Continuous Galerkin P1P4 elements are chosen for spatial discretization of the $(\hat{\rho}, \hat{u})$ function space. This is the lowest polynomial order function space which results in a smooth solution, and doesn't result in spurious oscillations. Further investigation of the discretization scheme stability and consistency must be performed.

4.2.1 General approach

To demonstrate the discussed shape optimization approach, we start with a simple geometry: a channel with a single adjustable boundary. We consider the restriction part of the generic inkjet printer geometry as the optimization boundary (fig. 4.1).

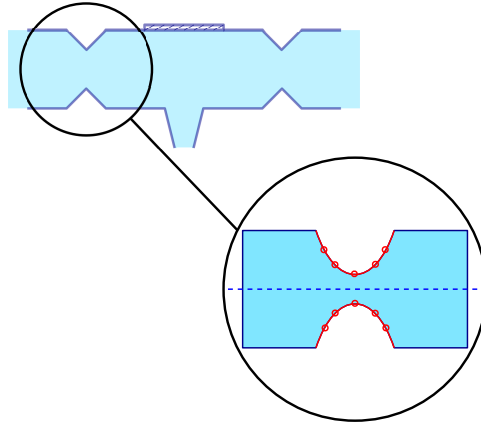
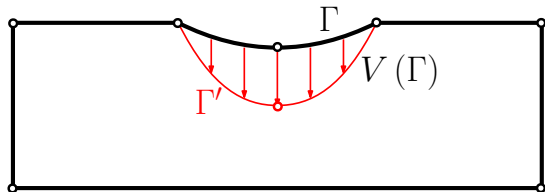


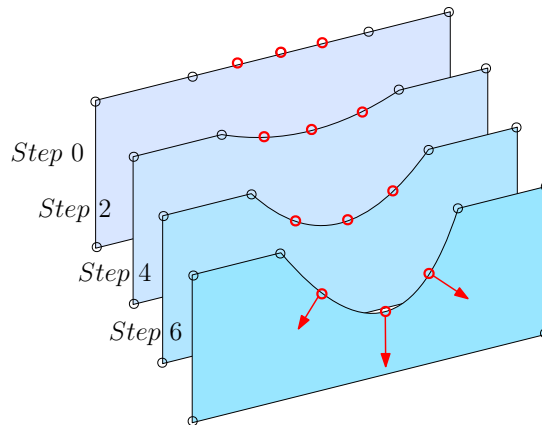
Fig. 4.1 Symmetric restriction part of the generic inkjet geometry as an optimization boundary.

We assume the restriction to be symmetric in horizontal plane, thus we can optimize only the upper part of the channel. The variable part of the boundary is parametrized by Bezier curve, and we calculate the sensitivity of the objective function to the positions of the control points. To illustrate this, consider a three-point boundary (fig. 4.2a), with the initial shape Γ and given displacement field $V(\Gamma)$. Only the middle point can move, while the other two are fixed. Otherwise, the adjacent boundaries will displace as well. Once the shift step size Δt of the middle point is calculated, its

position is moved in the steepest descent direction, and the domain boundary becomes $\Gamma' = \Gamma + \Delta t \cdot V$. For the real part of an eigenvalue $\Re(s)$ as the objective function, we expect the series of optimization steps to behave as illustrated in fig.4.2b.



(a) A boundary displacement $V(\Gamma)$ and a modified boundary ($\Gamma \rightarrow \Gamma'$) example.



(b) A series of shape optimization steps results in the restriction expansion.

We consider a rectangular channel with 7 control points to calculate the modes and the eigenvalues. The length and the height of the channel are 1.0 and 0.25, respectively; the dimensionless viscosity ν is 0.01. The displacement is applied to the top boundary in the range $x = [0.25, 0.75]$. Then, we apply gradient steps to stabilize the eigenvalue with the least non-zero frequency. To keep the no-slip boundary smooth, the y -coordinates of the two first and two last points are fixed. Figure 4.3 illustrates the spectra for different boundary shapes. The real part of the eigenvalues decrease on each iteration, by approximately 25% in total. Note that the frequency of each mode are almost the same as the frequencies of the 1D inviscid wave equation.

The boundary shape convergence is shown in figure 4.4. The next calculated top boundary's displacement overlaps the bottom slip boundary so we stop the iteration here. The control points and consequently the boundary shift down so the restricted area expands. This increases viscous dissipation inside the domain, making natural modes more stable, as expected. A practical optimization scheme would need to include further constraints, such as a limit on the mean flow viscous dissipation, which are not yet included here.

Figure 4.4 contains the density amplitude $|\hat{\rho}|$ of the first four natural modes. The first (left) column illustrates the modes of the initial unperturbed channel, while the following figures show the shape change of both the channel and the natural modes for the 4th, 6th and the final iteration of the shape optimization algorithm. Contours are equidistant for each mode.

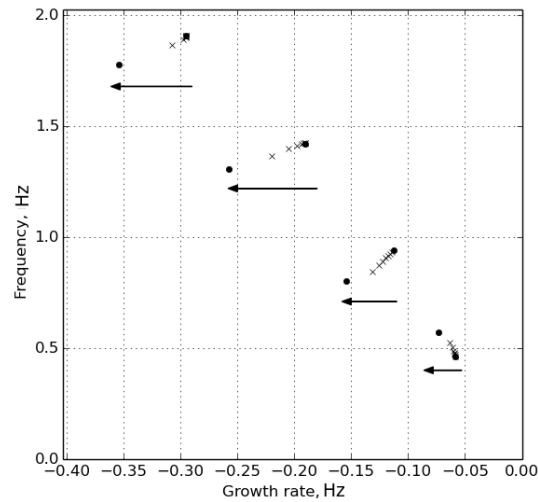


Fig. 4.3 Spectra of the channel for different shapes. Black dots correspond to the initial and the final eigenvalues, with intermediate steps in between. Arrows illustrate the direction of the spectrum shift.

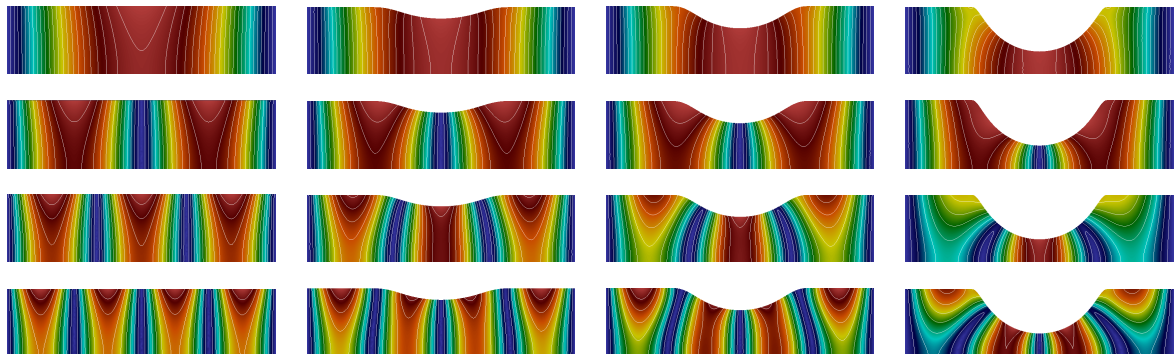


Fig. 4.4 Amplitude of the density variable, $|\hat{\rho}|$, for the four modes (from top to bottom) for various channel's shapes. Left column: unperturbed channel; right column: the final shape.

In order to verify the method, we also perform Taylor test analysis for adjoint gradients. For each of the boundary types (no slip, free and compliant) we plot the gradient-based deviation as proposed in (3.76) and (3.77). We parameterize each of the tested boundaries with three points (two fixed and one adjustable) and vary the middle point position. The following figures illustrate the deviation data and polynomial fitting (linear and quadratic): fig.4.5 contains a Taylor test for a no slip boundary displacement, with the real part of the adjoint gradient equals to 0.417 at $\Delta x = 0$. Figure 4.6 shows the Taylor test for a free boundary, the initial gradient equals to -0.0077. Figure 4.6 corresponds to a compliant boundary with non-dimensional impedance $Z = 20.0 + 20.0i$, and the initial gradient is 0.247.

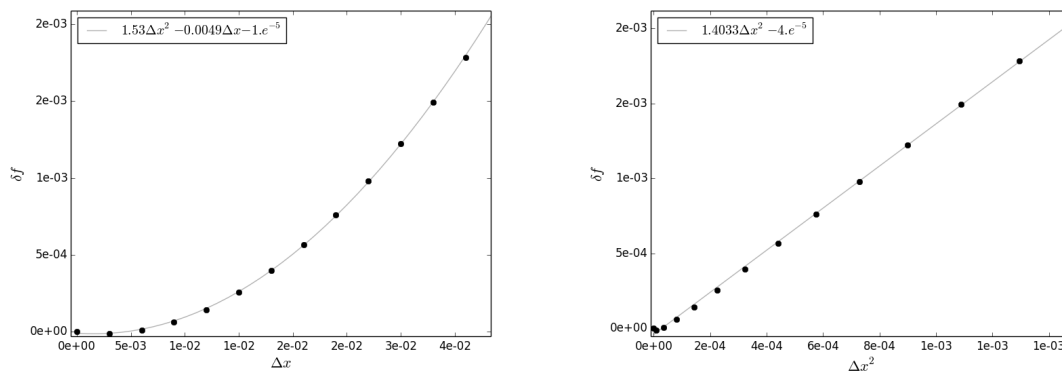


Fig. 4.5 Taylor tests for no slip boundary eigenvalue gradient, with quadratic and linear fitting.

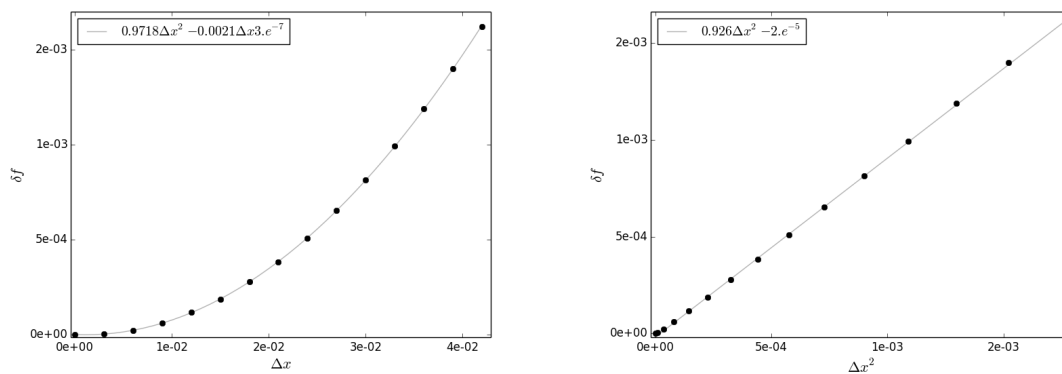


Fig. 4.6 Taylor tests for stress free boundary eigenvalue gradient, with quadratic and linear fitting.

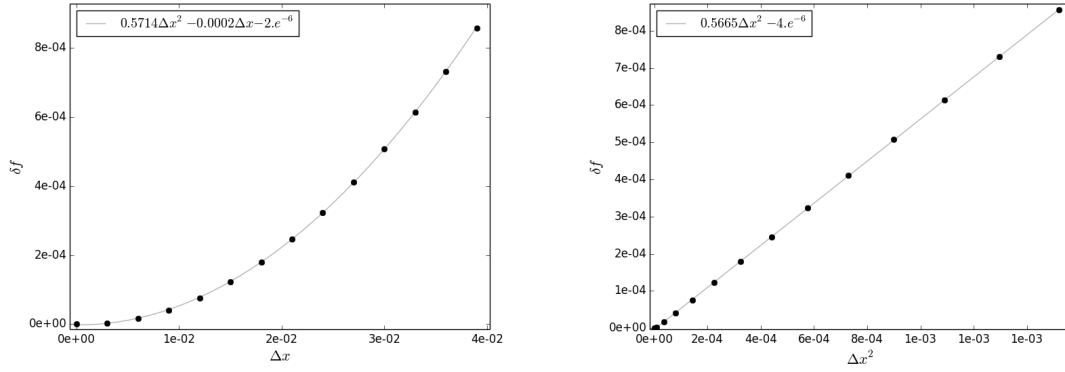


Fig. 4.7 Taylor tests for compliant boundary eigenvalue gradient, with quadratic and linear fitting.

4.2.2 Spectrum-based optimization

The gradient with respect to displacement of the objective function, the natural frequency of a system in our case, allows us to optimize not only the primary objective, but also any function of the objective(s): $\sigma = \sigma(s_1, s_2, \dots)$, since the gradient of the composite objective can be written as a linear combination of the primary gradients.

Let us consider a system with boundaries of a given shape. We aim to adjust the shape of the channel the way first several modes have *almost* the same real part of the eigenvalues. Physically, it corresponds to the case when dissipation rate of the system perturbations close to the chosen eigenvalues decay with nearly the same rate.

Since we want to minimize the difference between real parts of the set of eigenvalues, let us start with the trivial case of two different modes, with the eigenvalues s_1 and s_2 . Following the described approach, we calculate the shape derivative for both s_1, s_2 . We introduce a new cost function, σ , equal to the squared distance between the eigenvalues real parts.

$$\sigma = (\Re(s_1 - s_2))^2 \quad (4.1)$$

Then, the shape derivative $\sigma'[V]$ can be calculated using the given gradients, namely:

$$\sigma'[V] = 2\Re(s_1 - s_2)\Re(s_1'[V] - s_2'[V]) \quad (4.2)$$

Minimization of the distance means that $\sigma'[V] < 0$, so we can choose the direction of the displacement, V , basing on the sign of the product (4.2). Finally, the actual distance reduction becomes:

$$\Delta\sigma = 2\mathbb{R}(s_1 - s_2) \left(\mathbb{R}(s'_1[V]^i - s'_2[V]^i) \cdot V^i \right) \quad (4.3)$$

where $s'_{1,2}[V]^i, V^i$ are the gradient and the displacement value corresponding to the i -th control point.

4.3 Multi-objective shape optimization

4.3.1 General principle

The next example is optimization of a combination of different objective functions. We (again) consider the real part of the first eigenvalue as the first objective function, and viscous dissipation over the whole domain as the second one. Namely, the (weighed) multiobjective function can be written as:

$$\mathcal{J}_w = c_1 \mathbb{R}(s_1) + c_2 Q \quad (4.4)$$

Here Q is the domain-averaged viscous dissipation of the steady flow, and $c_{1,2}$ are some constants. Now, the derivative of the multiobjective cost function is:

$$\mathcal{J}'_w[V] = c_1 \mathbb{R}(s'_1[V]) + c_2 Q'[V] \quad (4.5)$$

We want to 1) reduce the lifetime of the acoustic waves propagating inside the channel, thus decrease the real part of the eigenvalue; 2) decrease the pressure drop in the channel due to the presence of the restriction, which is essentially the viscous dissipation of the flow's energy. Now the tricky part of the problem arises from the similarity of these two physical phenomena, each of them represents viscous dissipation in the flow. The decay rate increases as the channel expands, $\mathbb{R}(s'_1[V]) > 0$, while the viscous dissipation becomes lower, $Q'[V] < 0$. In other words, at first sight we want to both increase viscous dissipation (decay rate $\mathbb{R}(s_1)$) and decrease it (viscous dissipation Q itself) at the same time, which seems impossible.

Another possible problem statement is to minimize the following expression instead:

$$\mathcal{J}_w = -\frac{Q}{\mathbb{R}(s_1)} \quad (4.6)$$

It is positive ($Q > 0, \mathbb{R}(s_1) < 0$), and we don't have any coefficients as we had previously. The shape derivative is straightforward:

$$\mathcal{J}'_w[V] = -\frac{Q}{\mathbb{R}(s_1)} \left(\frac{Q'[V]}{Q} - \frac{\mathbb{R}(s'_1[V])}{\mathbb{R}(s_1)} \right) \quad (4.7)$$

Now the described conceptual problem becomes more clear: *if the relative decay rate change equals to the relative change of the viscous dissipation for any displacement, then it is impossible to find an optimal solution which minimizes target objective function.*

4.3.2 Pareto optimality

One question can be asked at this point: how can one decide upon the choice of the weighing constants or the normalization type? Usually this knowledge comes from outside of the model, for example, as a manufacturing cost or an importance of a certain design feature. But even without knowing the exact way to construct the *weighed* objective function, \mathcal{J}_w , one can still improve the objective function by searching for a Pareto frontier of the problem.

Pareto optimality yields that there is no possible change can be made to improve one objective function without worsening any other objective. Note, that this definition doesn't require the combination of the objective functions, so it is possible to treat them separately. When the Pareto frontier is found (meaning that we know the location of the Pareto optimal solutions) we can finally apply the exact values of the weighing coefficients and choose the best solution.

Fig. 4.8 illustrates the example of a single optimization iteration. Consider we have two objective functions, J_1, J_2 as functions of (x, y) and we know their gradients, $\nabla J_1, \nabla J_2$. In the case of the fully-known system, the weights are defined as $\alpha_{1,2}$, and our generalized weighed objective function J_w will move in the direction ∇J_w (red arrow). It essentially means that we are solving a single-objective optimization problem.

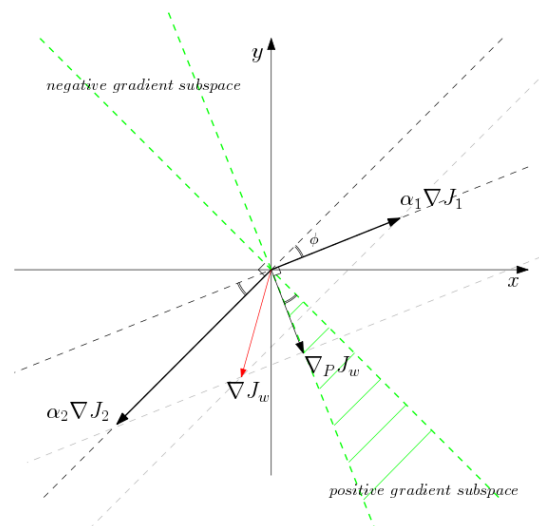


Fig. 4.8 Gradients of two objective functions J_1, J_2 with non-zero angle ϕ between the gradient directions (dashed lines) form a positive gradient subspace (green area), such that a possible gradient step exists which improves both the objectives.

However, without the weights information, we still have the gradients direction (dashed lines), so by forming a positive gradient subspace, the possible improvements are allocated. If the angle between the gradient directions is non-zero, the Pareto-optimal solutions have not been reached yet. This condition can be formulated as:

$$\cos(\phi) = \frac{(\nabla J_1, \nabla J_2)}{\|\nabla J_1\| \cdot \|\nabla J_2\|} > -1 \quad (4.8)$$

Any direction within the positive gradient subspace can be chosen for the gradient descent method, and taking one on the surface of the subspace corresponds to keeping the forming objective constant. The cone angle ϕ equals to that between the gradients directions. If $\cos(\phi)$ is positive, then any positive linear combination of the gradient vectors result in the objective functions improvement. The larger the cosine value is, the larger the generalized cost function's increment can be achieved. Once the angle becomes zero, the Pareto frontier is reached.

Another noticeable approach is that if we know the weights the positive gradient subspace can still be useful. By projecting the weighed gradient ∇J_w to the closest subspace surface (or boundary), the projected gradient $\nabla_P J_w$ is obtained and the next optimization step will both improve the generalized objective function and keep all the individual objectives nearly the same without worsening them.

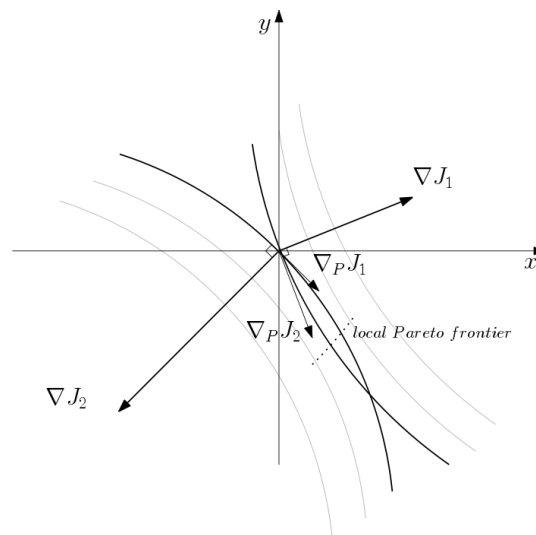


Fig. 4.9 Isolines of two functions intersect and create a region with a local Pareto frontier inside it. Two projected gradient vectors bound the area inside which both J_1 and J_2 increase.

Fig. 4.9 illustrates an example of two cost functions while the Pareto optimum is not reached yet. Two black curves correspond to the functions' isolines; the intersection

region exists and is bounded by two projected gradients, $\nabla_P J_1, \nabla_P J_2$. Since the intersection is non-zero, there appears to be a local Pareto frontier (dotted line) in the direction of the both projected gradients. By choosing a certain step direction, one will finally reach an optimal point located in the subspace formed by the projected gradients. For instance, one can choose the gradient step as follows:

$$d\mathbf{R} = \text{proj} \left(\frac{\nabla J_1}{|\nabla J_1|}, \nabla^\perp J_2 \right) + \text{proj} \left(\frac{\nabla J_2}{|\nabla J_2|}, \nabla^\perp J_1 \right) \quad (4.9)$$

Here *proj* is a projection operator of the first vector argument in the direction of the second; and $^\perp$ is an orthogonal direction to a vector.

4.3.3 Approaching Pareto frontier

Now, we will apply the discussed idea to a 2D internal flow in a channel with two asymmetric restrictions (fig.4.10), parameterised by 6 control points. By asymmetric we assume the possibility to apply different shape changes depending on the actual calculated gradients. Initial restriction shape (black dashed curves) can change differently and shift to the red dashed lines. The shift of the control points of the left and right boundaries can be different, e.g. from the black dots to the red dots. The physical reason behind the asymmetry lies in the asymmetry of the flow field, which defines the viscous dissipation cost function: the first restriction produces a higher velocity gradient than the second one. On the other hand, since the channel initial shape is symmetric, the eigenvalue-based cost function creates a displacement field equal for the right hand side and left hand side restrictions.

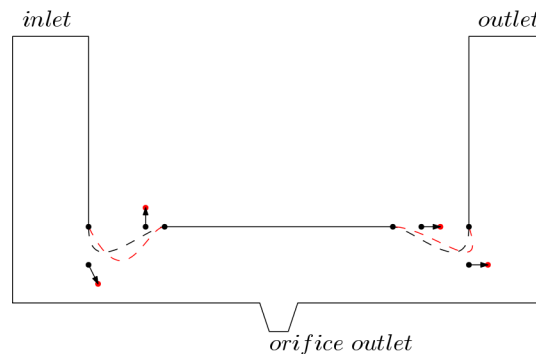


Fig. 4.10 Symmetric channel with two asymmetric restrictions. Black dots and dashed lines illustrate initial position of control points and smooth boundaries; red show those after a gradient step was applied.

To illustrate this principle, we plot shape gradients normalized by the cost function values (fig.4.11a,4.11b). Fig.4.11a shows the normalized gradients of the real part of the first eigenvalue (red dots) and viscous dissipation (green dots) for four control points of the left restriction. The filled areas imply the cone angle ϕ , with almost zero for the third and fourth points and 8° and 3° for the first and second. It means, that the improvement towards the Pareto optimum can still be made by applying a gradient step for the control points with non-zero gradient subspace. However, the angles are too small to result in efficient optimization.

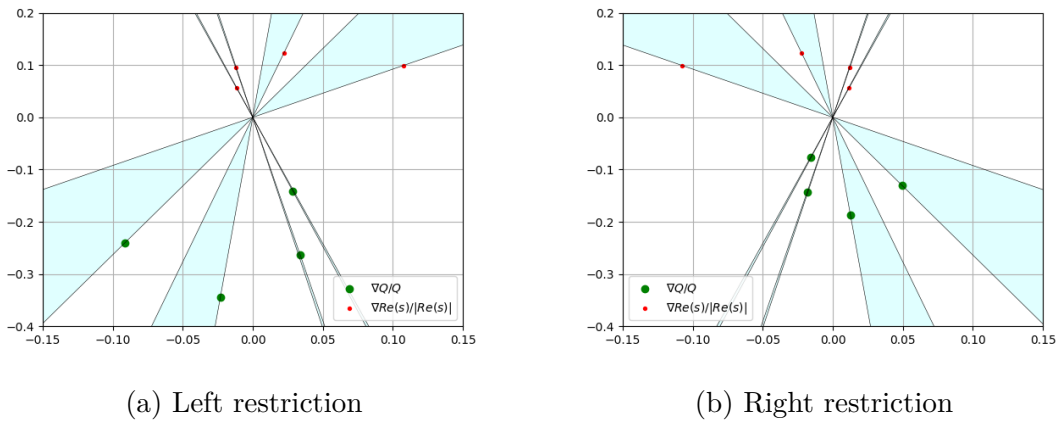


Fig. 4.11 Normalized gradient directions for viscous dissipation (green dots) and real part of the first eigenvalue (red dots) for four control points of the restriction boundaries.

Fig.4.11b illustrates the normalized gradient of the right hand side restriction. The eigenvalue displacement directions are identical to those of the left boundary, while the gradients of the second cost function are different. The right hand side restriction produces less viscous dissipation, thus the sensitivities are smaller.

4.4 Inkjet printhead optimization

The inkjet printhead feature we discuss here is the shape of two restrictions located between the ink chamber with oscillating piezo boundary, and the inlet. When the frequency of an external periodic forcing acting on the fluid becomes high enough, namely equal to or the order of the frequency of the first natural mode of the system, acoustic waves inside the chamber may exist for long enough to affect subsequent ink droplets' formation. Manufacturers would like to achieve working frequencies of hundreds of kilohertz, which is close to the first eigenvalue, and therefore in this range. Presence of the restriction should help acoustic waves to dissipate or propagate away quickly and thus not to affect the next oscillation. Future optimization may try to increase this natural frequency, subject to geometrical constraints.

4.4.1 Generic geometry

Fig. 4.13 shows top and side view of the generic inkjet printhead geometry. This initially symmetric channel has an inlet and outlet, an orifice at the bottom, and an adjustable restriction boundary. Shaded walls can be either no slip or compliant boundaries; all the results below are obtained with the no slip condition. The orifice represents an open end, where droplets are formed.

While in general it is not restricted to optimize the whole geometry at once, we focus on the highlighted part only. The bottom two-dimensional channel is chosen as the model geometry. We assume, that it covers all the necessary features of the full three-dimensional case.



Fig. 4.12 The Xaar 1003 AMp printhead [42].

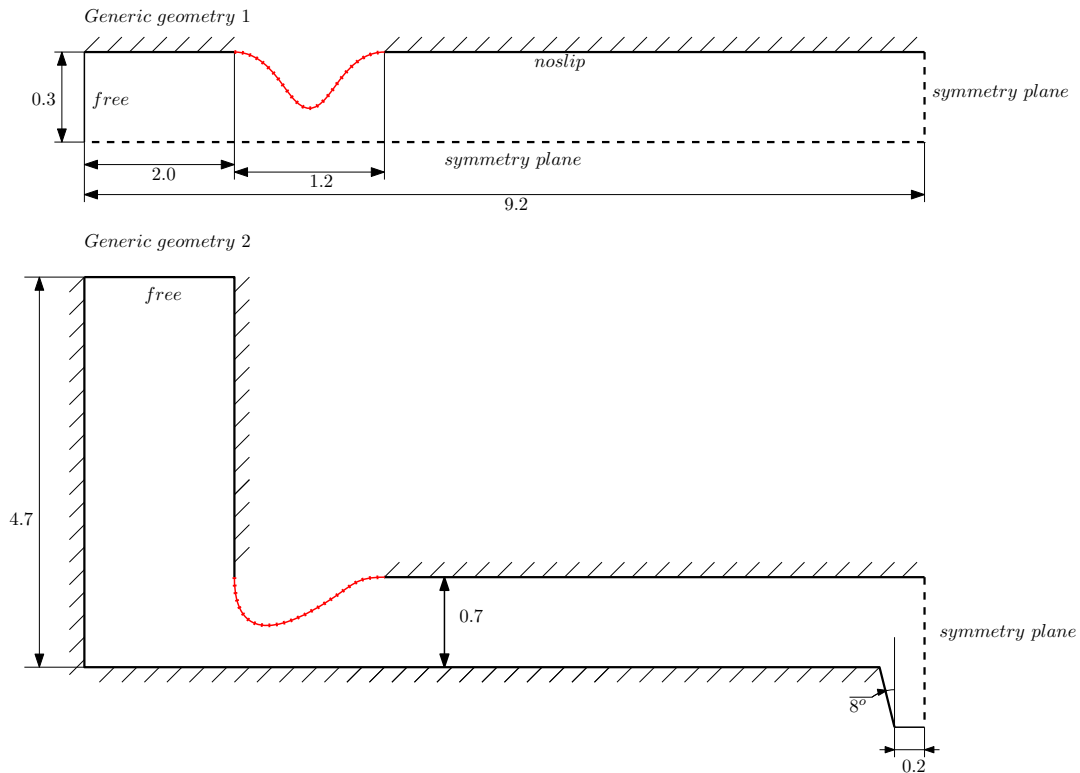


Fig. 4.13 Generic geometry of the inkjet printhead (top and side view). Straight shaded lines correspond to no slip or compliant boundaries, dashed lines are planes of symmetry, and free boundaries as specified. Two red dotted lines denote restriction boundaries subject to optimization. All sizes in $100\mu\text{m}$.

4.4.2 Optimization results

We start with the parametrization of two side parts of the upper boundary with four Bezier control points. The space between them represents the piezo element boundary, which should be kept plane.

The initial geometry and the first mode are illustrated in fig. 4.14. The density mode amplitude $|\hat{\rho}|$ (4.14a) and velocity amplitudes $|\hat{u}_{x,y}|$ (4.14b,4.14c) show, that the lowest frequency mode corresponds to a wavelength twice the length of the duct, and the velocities and hence viscous dissipation are greatest around the sharp corners and in the orifice outlet, as expected. Consequently, the choice of the optimization region is justified. The frequency of the mode is 340 kHz and the decay rate is almost 14 kHz, which is in a good agreement with the experimental data provided by the manufacturer.

We apply gradient steps to the left boundary first (fig.4.15), and then to the right boundary (fig.4.16a). After the first optimization stage decay rate increases to just

above 16 kHz, and to almost 19 kHz after the second stage. Overall, the decay rate increased by approximately 25% (4.17a). The frequency of the mode dropped to slightly less than 330 kHz.

Fig. 4.17b illustrates the shifts of each of two adjustable control points in xy plane. The blue dots correspond to the left boundary, and the red to the right boundary. While the total height of the channel is 0.7, the control points shifted down almost to the lower channel boundary. Note, that for both cases control points followed almost the same optimization trajectory, as expected from the problem symmetry.

The decay rate growth naturally leads to viscous dissipation increase and therefore pressure drop inside the channel for the mean flow. We are developing an extension to the presented model so to take into account the presence of the pressure difference on the inlet and outlet of the channel and to solve the joint minimization problem.

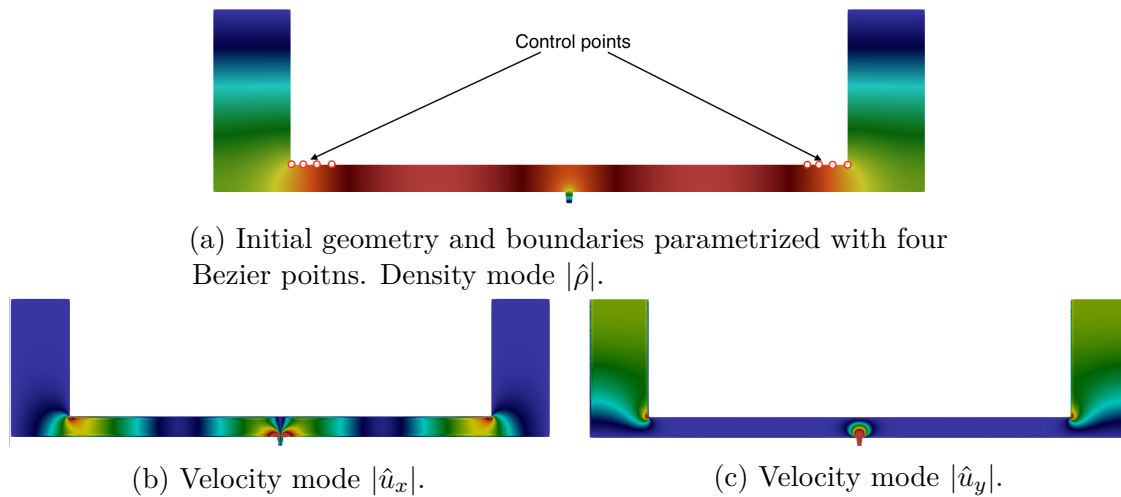


Fig. 4.14 Initial channel geometry and the lowest frequency mode.

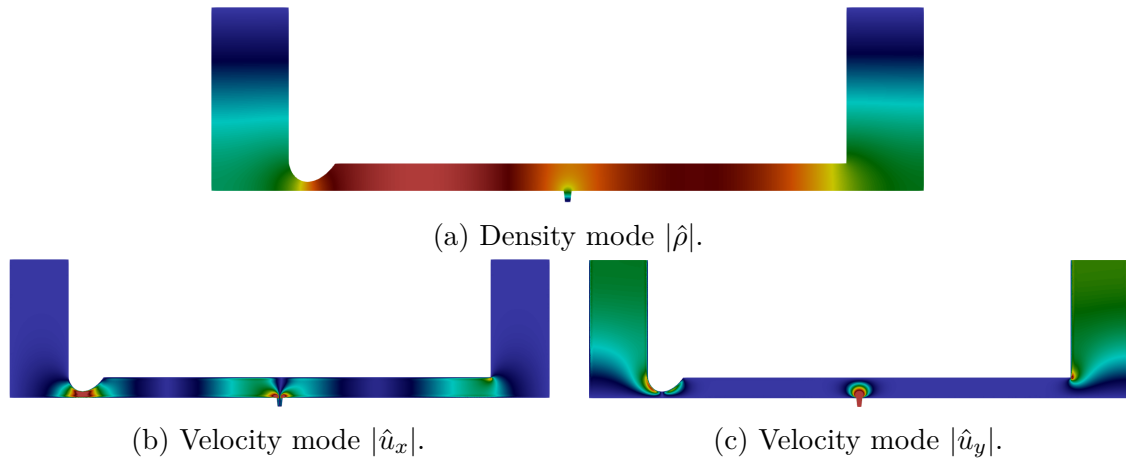


Fig. 4.15 Channel geometry with the optimized left hand side constriction and the lowest frequency mode.

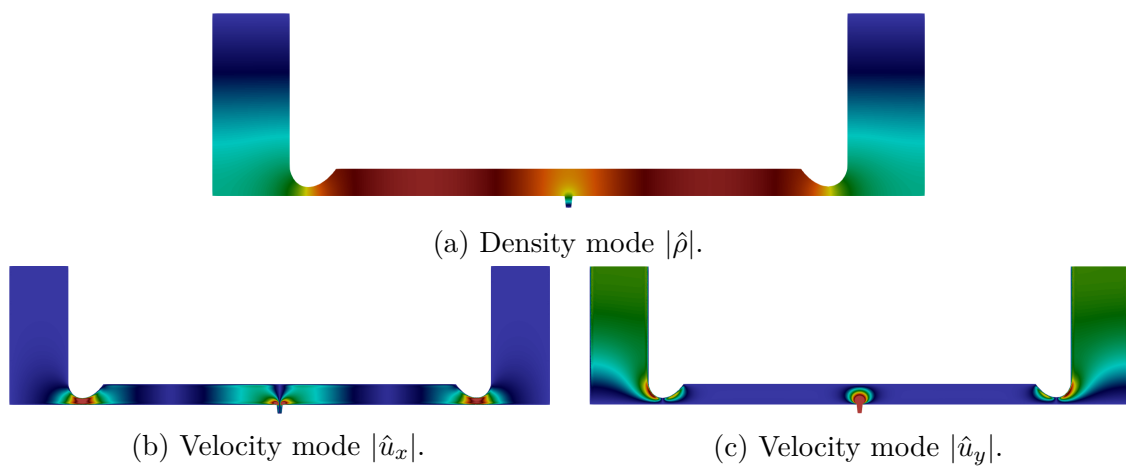
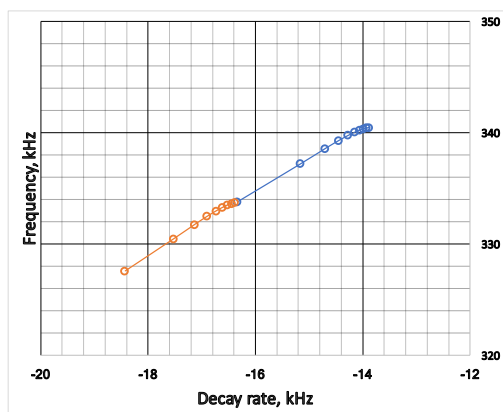
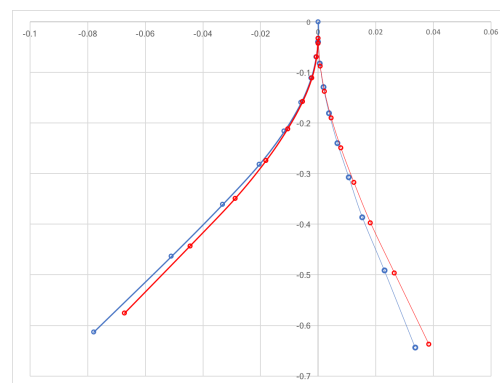


Fig. 4.16 Channel geometry with two optimized constrictions and the lowest frequency mode.



(a) The first natural frequency of the system for different shape configurations. Blue dots correspond to the first optimization stage (left restriction), and red dots to the second stage (right restriction).



(b) The shifts of two adjustable control points in xy plane for the left hand side restriction (blue lines) and the right hand side restriction (red lines).

4.5 Shape optimization for viscous dissipation

In this section we briefly discuss viscous dissipation shape sensitivity for unsteady incompressible flow. We consider a generic printhead geometry with single constriction, with time-dependent inlet velocity profile. We aim to illustrate the periodic behaviour of the direct and adjoint flows, and deduce a generic optimization strategy.

The initial condition is $u(x, t = 0) = 0$, and the inlet boundary condition is $u_{in}(t) = (1 - e^{-t/\tau})(1 + 0.1\sin(2\pi t))$, $\tau = 0.285$. The flow becomes periodic after sufficiently long time, smoothly reaching the periodic solution. Fig. (4.18) illustrates the inlet velocity amplitude and viscous dissipation from $t = 0$ to $t = 4$. Viscous dissipation is normalized by its mean value, and it reaches periodic solution together with the inlet velocity profile. The shape gradient experiences periodic behaviour as well.

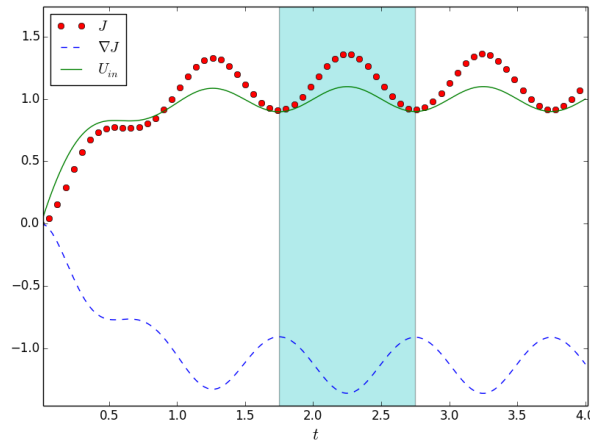


Fig. 4.18 Inlet velocity profile, viscous dissipation and shape gradient of unsteady flow in a channel. Shaded area illustrates the proposed averaging interval for periodic flow.

The total gradient for the unsteady flow is obtained by integration over the whole time domain. If the transition region contribution is assumed to be small (for instance, if the flow oscillates hundreds of periods), it is reasonable to perform time averaging over just one oscillation period.

As shown before, viscous dissipation and the acoustic decay rate gradients and therefore optimal displacements have opposite directions, thus any configuration is (almost) Pareto-optimal. Therefore, we can only choose one optimization objective. In our case, viscous dissipation and the corresponding pressure drop inside the channel is less important than the acoustic stability, up to a certain threshold. When viscous dissipation approaches critical value, defined by a manufacturer, the optimization should terminate or the pressure drop should be added as a new constraint.

Chapter 5

Conclusion

5.1 Key results

This report shows the methodology and results of shape optimization for an inkjet printhead. We have performed a two-parameter expansion of the compressible Navier–Stokes equation considering mean and fluctuating motions at low Mach numbers. The full problem splits into the incompressible unsteady flow, and the viscous acoustic flow. For both these limits, strong and weak formulations have been proposed with corresponding sets of boundary conditions. An acoustic compliant boundary condition, relating the force and velocity fields on the boundary, has been implemented. This allows us to model boundaries that are not fixed and can displace, reacting to the flow. The computed first natural mode’s frequency is in a good agreement with the experimental data.

Using the adjoint approach, we have derived a general expression for the eigenvalues sensitivity of the natural modes for the viscous acoustic flow. The shape derivative in Hadamard form has been presented, as well as the Taylor (convergence) test for the adjoint-based gradients. We have applied shape optimization to the generic two-dimensional inkjet printhead geometry. The decay rate of the first natural mode was increased by approximately 25%, by modifying the channel’s constriction shape. The multiobjective shape optimization approach for pressure drop inside the channel and the acoustic flow stability has been discussed.

Finally, we have developed a generic solver for viscous dissipation and stability optimization, based on the open-source framework FEniCS. The solver includes a CAD-like geometry builder and allows us to run the optimization routine in several lines of code.

5.2 Future research

We propose the following work to be performed:

- Shape parameterization

The choice of shape parameterization seems to be crucial for shape optimization. In the current research we use Bezier parameterization, which is very useful for maintaining boundary smoothness and can be virtually infinitely flexible given an appropriate number of control points. We aim to compare different parameterization techniques, especially their convergence rates for shape optimization problems.

- Three-dimensional shape optimization

In practical applications, the flow is 3D, while the shape optimization has been performed in 2D case. To prove the consistency of the results, a full 3D test case should be considered.

- Impedance and compliant boundary

Acoustic boundary impedance depends on boundary properties, known from experimental data and the fluctuation frequency $Z = Z(s)$. The eigenvalue problem then becomes nonlinear, and the iterative algorithm should be applied. This is necessary for accurate caption of physical effects inside the channel, such as fluid–structure interaction and wave propagation.

- Multiphase effects on the meniscus surface

As discussed before, the multiphase physics of droplet formation is one of the governing mechanisms of inkjet printing technology. Currently we consider only the stress-free boundary condition at the nozzle, thus a more sophisticated model should be considered. It is necessary to investigate the influence of surface tension and the meniscus shape on the acoustic flow and the system's stability.

- Discretization consistency

Spatial discretization and the choice of function spaces determine the numerical scheme stability and consistency. We should perform a thorough analysis on the numerical scheme and validate the implemented approach.

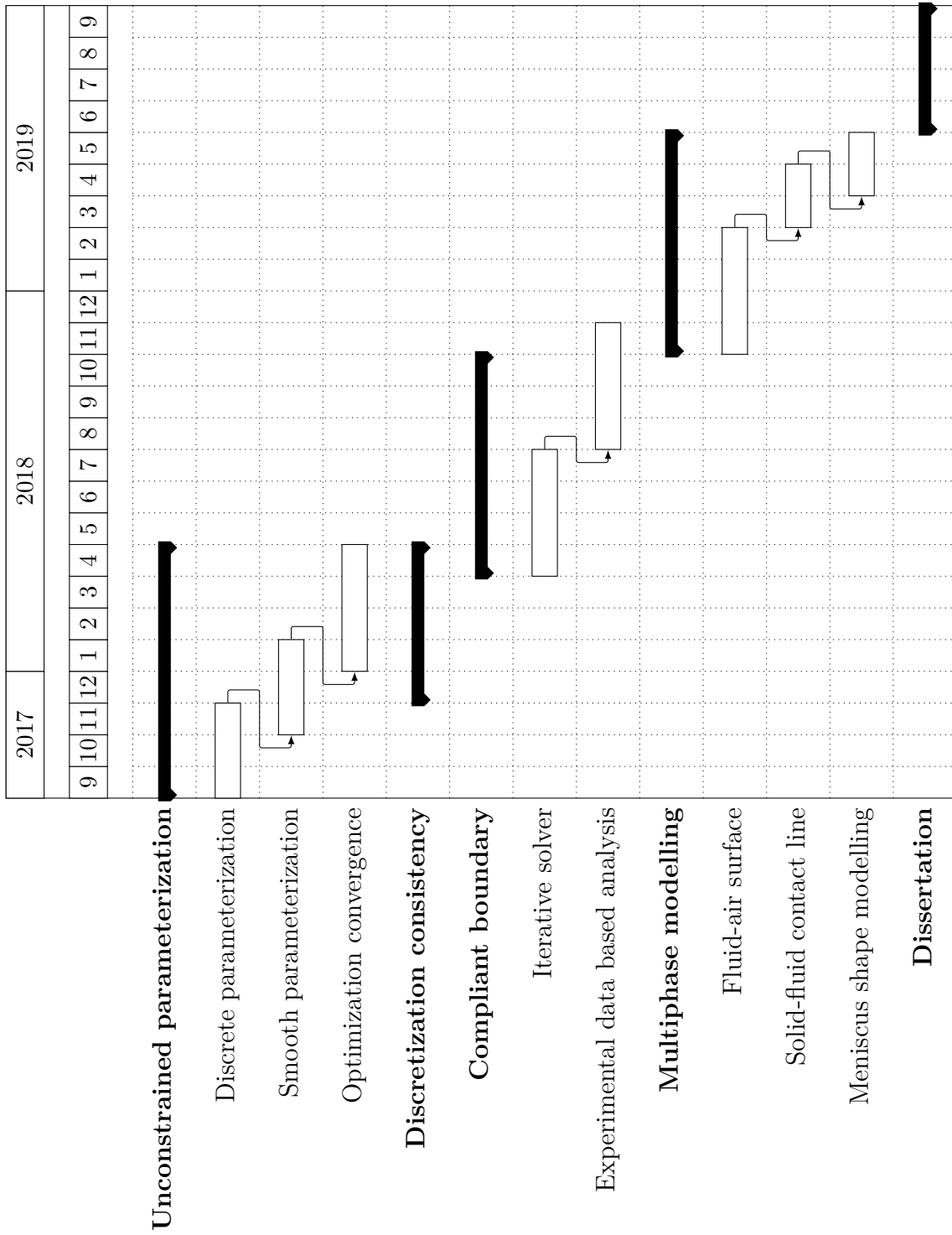


Fig. 5.1 Gantt chart

References

- [1] Bogy, D. B. and Talke, F. E. (1984). Experimental and theoretical study of wave propagation phenomena in drop-on-demand ink jet devices. *IBM J. Res. Dev.*, 28(3):314–321.
- [2] Boyd, S. and Vandenberghe, L. (2004). *Convex Optimization*. Cambridge University Press.
- [3] Brewster, J. (2016). Shape optimization for linear stability. First year report, University of Cambridge.
- [4] Cossu, C. (2014). An introduction to optimal control. *Applied Mechanics Reviews*, 66(2).
- [5] Culick, F., Kuentzmann, P., RESEARCH, N., and (France), T. O. N.-S.-S. (2006). *Unsteady Motions in Combustion Chambers for Propulsion Systems*. Defense Technical Information Center.
- [6] Delfour, M. C. and Zolésio, J.-P. (2001). *Shapes and Geometries: Analysis, Differential Calculus, and Optimization*. Society for Industrial and Applied Mathematics, Philadelphia, PA, USA.
- [7] Donea, J., Giuliani, S., and Halleux, J. (1982). An arbitrary lagrangian-eulerian finite element method for transient dynamic fluid-structure interactions. *Computer Methods in Applied Mechanics and Engineering*, 33:689–723.
- [8] Donea, J., Giuliani, S., Laval, H., and Quartapelle, L. (1982). Finite element solution of the unsteady navier-stokes equations by a fractional step method. *Computer Methods in Applied Mechanics and Engineering*, 30(1):53 – 73.
- [9] Donea, J., Huerta, A., Ponthot, J.-P., and Rodríguez-Ferran, A. (2004). *Arbitrary Lagrangian–Eulerian Methods*, chapter 14. John Wiley & Sons, Ltd.
- [10] Freund, J. and Stenberg, R. (1995). On weakly imposed boundary conditions for second order problems. In *Proceedings of the Ninth Int. Conf. Finite Elements in Fluids*, pages 327–336. Venice.
- [11] Gao, Z. and Ma, Y. (2010). Unsteady flow optimization by a stabilized finite element method. *International Journal for Numerical Methods in Biomedical Engineering*, 26(12):1915–1933.
- [12] Gao, Z., Ma, Y., and Zhuang, H. (2006). Optimal Shape Design for the Time-dependent Navier–Stokes Flow. *ArXiv Mathematics e-prints*.

- [13] Giles, M. B. and Pierce, N. A. (2000). An introduction to the adjoint approach to design. *Flow, Turbulence and Combustion*, 65(3):393–415.
- [14] Hartmann, R. (2008). Numerical analysis of higher order discontinuous galerkin finite element methods. In *VKI Lecture series 2008-08, 35th CFD/ADIGMA course on very high order discretization methods*. Von Karman Institute for Fluid Dynamics, Rhode Saint Genese, Belgium.
- [15] Homescu, C., Navon, I. M., and Li, Z. (2002). Suppression of vortex shedding for flow around a circular cylinder using optimal control. *International Journal for Numerical Methods in Fluids*, 38(1):43–69.
- [16] Jameson, A. (1988). Aerodynamic design via control theory. *Journal of Scientific Computing*, 3(3):233–260.
- [17] Juniper, M. P. (2015). Adjoint and Passive Control in Thermoacoustics. *21st CISM-IUTAM International Summer School on Measurement, Analysis, and Passive Control of Thermoacoustic Oscillations*.
- [18] Juntunen, M. and Stenberg, R. (2009). Nitsche’s method for general boundary conditions. *Math. Comput.*, 78(267):1353–1374.
- [19] Khalate, A., Bombois, X., Babuska, R., Wijshoff, H., and Waarsing, R. (2010). *Optimization-based feedforward control for a Drop-on-Demand inkjet printhead*. Proceedings of the 2010 American Control Conference, ACC 2010.
- [20] Khalate, A. A., Bombois, X., Babuška, R., Wijshoff, H., and Waarsing, R. (2011). Performance improvement of a drop-on-demand inkjet printhead using an optimization-based feedforward control method. *Control Engineering Practice*, 19(8):771 – 781.
- [21] Kungurtsev, P. V. (accessed August 23, 2017). *MeFlAd, the FEniCS-based solver*, <https://github.com/Corwinpro/MeFlAd>.
- [22] Kungurtsev, P. V. and Juniper, M. P. (Sep 13-15, 2017). Shape optimization for viscous acoustic flows in an inkjet printhead. In *International conference on evolutionary and deterministic methods for design optimization and control with applications to industrial and societal problems, Madrid, Spain*.
- [23] Kwon, K.-S. and Kim, W. (2007). A waveform design method for high-speed inkjet printing based on self-sensing measurement. *Sensors and Actuators A: Physical*, 140(1):75 – 83.
- [24] Landau and Lifshitz (1987). *Course of Theoretical Physics: Fluid Mechanics*. Pergamon.
- [25] Le, H. (1998). Progress and trends in ink-jet printing technology. *Journal of Imaging Science and Technology*, 42:49–62.
- [26] Logg, A., Mardal, K.-A., and Wells, G. N. (2012). *Automated Solution of Differential Equations by the Finite Element Method*. Springer.

- [27] Muller, B. (1999). Low mach number asymptotics of the navier-stokes equations and numerical implications.
- [28] Myers, M. K. (1980). On the acoustic boundary condition in the presence of flow. *Journal of Sound Vibration*, 71:429–434.
- [29] Nadarajah, S. and Jameson, A. (2001). Studies of the continuous and discrete adjoint approaches to viscous automatic aerodynamic shape optimization. In *15th AIAA Computational Fluid Dynamics Conference*, Fluid Dynamics and Co-located Conferences. American Institute of Aeronautics and Astronautics.
- [30] Nadarajah, S. and Jameson, A. (2002). Optimal control of unsteady flows using a time accurate method.
- [31] Nadarajah, S. K. and Jameson, A. (2007). Optimum Shape Design for Unsteady Flows with Time-Accurate Continuous and Discrete Adjoint Method. *AIAA Journal*, 45(7):1478–1491.
- [32] Nakazawa, T. and Azegami, H. (2016). Shape optimization of flow field improving hydrodynamic stability. *Japan Journal of Industrial and Applied Mathematics*, 33(1):167–181.
- [33] Nitsche, J. (1971). Über ein variationsprinzip zur lösung von dirichlet-problemen bei verwendung von teilräumen, die keinen randbedingungen unterworfen sind. *Abhandlungen aus dem Mathematischen Seminar der Universität Hamburg*, 36(1):9–15.
- [34] Rehm, R. G. and Baum, H. R. (1978). The equation of motion for thermally driven buoyant flows. *Journal of Research of the National Bureau of Standards*, 83(3):297–308.
- [35] Rienstra, S. and Hirschberg, A. (2017). *An Introduction to Acoustics*. Technische Universiteit Eindhoven.
- [36] Ronald D., J., Max D., G., Roy A., N., Gordon, E., and M. Yousuff, H. (1997). A self-contained, automated methodology for optimal flow control. Technical report.
- [37] Samareh, J. A. (2001). Survey of Shape Parameterization Techniques for High-Fidelity Multidisciplinary Shape Optimization. *AIAA Journal*, 39(5):877–884.
- [38] Schmidt, Stephan, S.-V. (2010). Shape derivatives for general objective functions and the incompressible navier-stokes equations. *Control and Cybernetics*, 39(3):677–713.
- [39] Shene, C.-K. (accessed August 23, 2017). *De Casteljau algorithm*, <http://www.cs.mtu.edu/shene/COURSES/cs3621/NOTES/spline/Bezier/de-casteljau.html>.
- [40] van der Meulen, M.-J. (2015). *Meniscus motion and drop formation in inkjet printing*. PhD thesis, Universiteit Twente.

- [41] Wijshoff, H. (2008). *Structure- and fluid-dynamics in piezo inkjet printheads*. PhD thesis.
- [42] Xaar (2016). *Leading Inkjet Innovation, Xaar application guide*. Xaar plc.
- [43] Yamaleev, N., Diskin, B., and J Nielsen, E. (2008). Adjoint-based methodology for time-dependent optimization. In *12th AIAA/ISSMO Multidisciplinary Analysis and Optimization Conference, MAO*.

Appendix A

Shape parameterization

A.1 Motivation

With a parameter-based shape optimization, it appears to be crucial to choose an appropriate parameterization of the shape. In some cases, the shape should be smooth or be symmetric, the number of bends can be limited due to the manufacturing complexity or the optimized boundary should only contain straight lines. A common example is the parameterization of an airfoil, which can be presented [37] as a number of boundary control points, a set of Bezier control points or only as several parameters defining the geometric properties, such as width or a front curvature radius. Usually, the chosen parameterization should be compatible with CAD systems.

In this research, we mainly consider only polynomial parameterization based on Bezier curves due to its flexibility and easy implementation. However, there exist a number of other options, for instance, B-splines or Fourier series. The last one, applied for various objective functions in viscous flows [3], results in a wavy boundary structure with many peaks, seems to be not very useful for industrial applications.

A.2 General properties

Any two dimensional boundary can be generally written as a function of internal coordinate t and a set of parameters, \mathbf{a} , such that $\mathbf{r} = \mathbf{R}(t, \mathbf{a})$. As for the Bezier curve, it is convenient to present it as a sum of Bernstein basis polynomials $b_{i,n}(t)$ weighed with the control points:

$$\mathbf{R}(t, \mathbf{a}) = \sum_{i=0}^n b_{i,n}(t) \mathbf{a}_i \quad (\text{A.1})$$

It is useful to note, that, first, the curve starts and ends at the first and the last control points; second, the slope of the curve at its boundaries is defined by the neighbor control point. For example, if the first and the second control points lie on a horizontal line, the slope is zero. This might be helpful if we want to impose a C_1 continuity at the connection points.

The displacement field, \mathbf{V} , is a response of a boundary shape to the change of a control parameters. In the case of a Bezier curve the displacement corresponding to the k -th control point \mathbf{a}_k equals to \mathbf{V}_k :

$$\mathbf{V}_k(t) = \frac{\partial \mathbf{R}}{\partial \mathbf{a}_k} = b_{k,n}(t) \quad (\text{A.2})$$

While the displacement notation is straightforward, there is not direct way to express it as a function of coordinates, \mathbf{r} . Thus one should apply additional numerical algorithms to construct the perturbed boundary.

A.3 Constructing a Bezier boundary

Generation of a Bezier boundary consists of two parts: creation of a boundary points set (the direct problem), and getting the internal coordinate, t , of a point on the boundary.

The direct step can be performed by either simply plugging an internal coordinate value into (A.1), or by using the De Casteljau's algorithm. While the first approach might include numerical errors while computing the Bernstein polynomials, the second algorithm has exponential complexity [39] thus limits the efficiency of the whole optimization routine. This is especially important when the number of surface vertices is high.

The implemented boundary generator creates a boundary point (x_i, y_i) , $i \leq N_b$ for each $t_i \in [0, 1]$, where N_b is a number of elements on the optimization boundary and t_i are equidistant internal boundary coordinates. This is equivalent to the quality of the mesh discretization. The inverse algorithm searches for t corresponding to the given point by iteration over the stored list of boundary vertices. Thus, if we want to create a pair of $(point, displacement)$, we first calculate the internal coordinate t matching the given position, and then apply (A.2) and assign its value to the *point*.

Appendix B

Complex eigenvalue problem in FEniCS

The finite elements package used does not support complex matrix operation. Complex terms can appear, for instance, if surface integrals contain the acoustic impedance value, which in general is complex. Additionally, complex matrices arise if one performs a complex shift in an eigenvalue problem. This problem can be resolved by splitting the the governing equations into the real and imaginary parts and solving $2N \times 2N$ real matrix instead of $N \times N$ complex matrix. The method presented below was proposed by Jack Brewster [3], and is described here for the educational purpose.

Consider a general eigenvalue problem. Without loss of generality, let $\mathbf{A} \in \mathbb{C}^N \times \mathbb{C}^N$ be a complex, and $\mathbf{B} \in \mathbb{R}^N \times \mathbb{R}^N$ be a real matrix. The generalized linear problem is to find an eigenvector $x \in \mathbb{C}^N$ and an eigenvalue $\lambda \in \mathbb{C}$, such that:

$$\mathbf{A}x = \lambda\mathbf{B}x \quad (\text{B.1})$$

We separate out the real and imaginary parts of the variables, $\mathbf{A} = \mathbf{A}_r + i\mathbf{A}_i$, $x = x_r + ix_i$, and $\lambda = \lambda_r + i\lambda_i$. The problem becomes:

$$\mathbf{A}_r x_r - \mathbf{A}_i x_i = \lambda_r \mathbf{B} x_r - \lambda_i \mathbf{B} x_i, \quad (\text{B.2a})$$

$$\mathbf{A}_r x_i + \mathbf{A}_i x_r = \lambda_r \mathbf{B} x_i + \lambda_i \mathbf{B} x_r \quad (\text{B.2b})$$

Or, in the matrix form:

$$\begin{bmatrix} \mathbf{A}_r & -\mathbf{A}_i \\ \mathbf{A}_i & \mathbf{A}_r \end{bmatrix} \begin{bmatrix} x_r \\ x_i \end{bmatrix} = \begin{bmatrix} \lambda_r I & -\lambda_i I \\ \lambda_i I & \lambda_r I \end{bmatrix} \begin{bmatrix} \mathbf{B} & 0 \\ 0 & \mathbf{B} \end{bmatrix} \begin{bmatrix} x_r \\ x_i \end{bmatrix} \quad (\text{B.3})$$

By introducing new matrix variables $\Gamma, M \in \mathbb{R}^{2N} \times \mathbb{R}^{2N}$, the equation (B.3) reads as:

$$\Gamma \begin{bmatrix} x_r \\ x_i \end{bmatrix} = \begin{bmatrix} \lambda_r I & -\lambda_i I \\ \lambda_i I & \lambda_r I \end{bmatrix} M \begin{bmatrix} x_r \\ x_i \end{bmatrix} \quad (\text{B.4})$$

Now, let us consider a new eigenvalue problem:

$$\Gamma y = \xi M y \quad (\text{B.5})$$

In general, the eigenvector $y \in \mathbb{C}^{2N}$ and eigenvalue ξ are complex; let us split the eigenvalue as $y = (y^1, y^2)$, where $y^{1,2} \in \mathbb{C}^N$. Since Γ is real by construction, the following is true:

$$\Gamma \begin{bmatrix} y_r^1 \\ y_r^2 \end{bmatrix} = \xi_r M \begin{bmatrix} y_r^1 \\ y_r^2 \end{bmatrix} - \xi_i M \begin{bmatrix} y_i^1 \\ y_i^2 \end{bmatrix}, \quad (\text{B.6a})$$

$$\Gamma \begin{bmatrix} y_i^1 \\ y_i^2 \end{bmatrix} = \xi_r M \begin{bmatrix} y_i^1 \\ y_i^2 \end{bmatrix} + \xi_i M \begin{bmatrix} y_r^1 \\ y_r^2 \end{bmatrix} \quad (\text{B.6b})$$

Then, it is trivial that

$$\Gamma \begin{bmatrix} -y_i^2 \\ y_i^1 \end{bmatrix} = \xi_r M \begin{bmatrix} -y_i^2 \\ y_i^1 \end{bmatrix} + \xi_i M \begin{bmatrix} -y_r^2 \\ y_r^1 \end{bmatrix} \quad (\text{B.7})$$

And combining (B.6a) and (B.7), we obtain:

$$\Gamma \begin{bmatrix} y_r^1 - y_i^2 \\ y_r^2 + y_i^1 \end{bmatrix} = \xi_r M \begin{bmatrix} y_r^1 - y_i^2 \\ y_r^2 + y_i^1 \end{bmatrix} + \xi_i \begin{bmatrix} 0 & -B \\ B & 0 \end{bmatrix} \begin{bmatrix} y_r^1 - y_i^2 \\ y_r^2 + y_i^1 \end{bmatrix} = \begin{bmatrix} \xi_r I & -\xi_i I \\ \xi_i I & \xi_r I \end{bmatrix} M \begin{bmatrix} y_r^1 - y_i^2 \\ y_r^2 + y_i^1 \end{bmatrix} \quad (\text{B.8})$$

Direct consideration of (B.4) and (B.8) shows, that the problems are equivalent, if $x_r = y_r^1 - y_i^2$ and $x_i = y_r^2 + y_i^1$, and $\lambda = \xi$. Thus, instead of solving the initial eigenvalue problem with complex matrices, we can solve the paired real-valued problem (B.5) instead.

Finally, consider a spectral shift in the complex plane is required, namely $\lambda \rightarrow \lambda + \lambda_0$, $\lambda_0 \in \mathbb{C}$. Then, the problem reads

$$(\mathbf{A} - \lambda_0 \mathbf{B})x = \lambda \mathbf{B}x \quad (\text{B.9})$$

And the split matrix form becomes:

$$\begin{bmatrix} \mathbf{A}_r - \lambda_{0,r}\mathbf{B} & -(\mathbf{A}_i - \lambda_{0,i}\mathbf{B}) \\ \mathbf{A}_i - \lambda_{0,i}\mathbf{B} & \mathbf{A}_r - \lambda_{0,r}\mathbf{B} \end{bmatrix} \begin{bmatrix} x_r \\ x_i \end{bmatrix} = \begin{bmatrix} \lambda_r I & -\lambda_i I \\ \lambda_i I & \lambda_r I \end{bmatrix} \begin{bmatrix} \mathbf{B} & 0 \\ 0 & \mathbf{B} \end{bmatrix} \begin{bmatrix} x_r \\ x_i \end{bmatrix} \quad (\text{B.10})$$

We have shown, that the complex spectral shift results in the change of Γ , keeping the problem structure the same.

Summing up, following the described approach, it is possible to project a $N \times N$ initial eigenvalue problem with complex-valued matrices into a $2N \times 2N$ real problem. The eigenmodes of the initial problem are a non-trivial linear combination of the the transformed problem eigenmodes.

